JOURNAL OF GEOPHYSICAL RESEARCH, VOL. 103, NO. D12, PAGES 13,837-13,857, JUNE 27, 1998

Radiative forcing from the 1991 Mount Pinatubo volcanic eruption

Georgiy L. Stenchikov,[1] Ingo Kirchner,[2] Alan Robock,[1,3] Hans-F. Graf,[2]
Juan Carlos Antuña,[1] R. G. Grainger,[4,5] Alyn Lambert,[4,6] and Larry Thomason[7]

Abstract. Volcanic sulfate aerosols in the stratosphere produce significant long-term solar and infrared radiative perturbations in the Earth's atmosphere and at the surface, which cause a response of the climate system. Here we study the fundamental process of the development of this volcanic radiative forcing, focusing on the eruption of Mount Pinatubo in the Philippines on June 15, 1991. We develop a spectral-, space-, and time-dependent set of aerosol parameters for 2 years after the Pinatubo eruption using a combination of SAGE II aerosol extinctions and UARS-retrieved effective radii, supported by SAM II, AVHRR, lidar and balloon observations. Using these data, we calculate the aerosol radiative forcing with the ECHAM4 general circulation model (GCM) for cases with climatological and observed sea surface temperature (SST), as well as with and without climate response. We find that the aerosol radiative forcing is not sensitive to the climate variations caused by SST or the atmospheric response to the aerosols, except in regions with varying dense cloudiness. The solar forcing in the near infrared contributes substantially to the total stratospheric heating. A complete formulation of radiative forcing should include not only changes of net fluxes at the tropopause but also the vertical distribution of atmospheric heating rates and the change of downward thermal and net solar radiative fluxes at the surface. These forcing and aerosol data are available for GCM experiments with any spatial and spectral resolution.

1. Introduction

Volcanic eruptions can inject into the stratosphere tens of teragrams of chemically and microphysically active gases and solid aerosol particles, which affect the Earth's radiative balance and climate and disturb the stratospheric chemical equilibrium. The volcanic cloud forms in several weeks by SO_2 conversion into sulfate aerosol and its subsequent microphysical transformations. The volcanic aerosols scatter visible solar radiation, reflect and absorb in the near-infrared (IR) bands, and absorb and emit thermal longwave (LW) radiation, providing significant radiative forcing of the climate system. The precise specification of this radiative forcing is very important for analysis of past observed climate variations and prediction of future climate changes. The perturbation of solar flux reaches several watts per square meter, lasts for more than a year, and causes surface temperature variations of up to 0.5°C [*Dutton and Christy*, 1992; *Minnis et al.*, 1993]. Observed variations of general circulation and climate include summer cooling and northern hemisphere winter warming near the surface, heating of the stratosphere by several degrees, enhancement of the northern polar vortex, and interaction with El Niño effects [*Robock and Mao*, 1992, 1995; *Graf et al.*, 1993; *Kirchner and Graf*, 1995; *Mao and Robock*, 1998].

On June 12-16, 1991, the Mount Pinatubo volcano on Luzon Island in the Philippines (15.1°N; 120.4°E) erupted several times, with the strongest explosion on June 15 producing the largest volcanic aerosol cloud in the stratosphere so far this century [*Bluth et al.*, 1992]. Within a few days of the eruption, total ozone mapping spectrometer (TOMS) observations [*Bluth et al.*, 1992] showed that the total stratospheric SO_2 injection was about 20 Mt. Later estimates from different authors ranged from 14 to 20 Mt [*McCormick and Veiga*, 1992; *Stowe et al.*, 1992; *Lambert et al.*, 1993; *Strong and Stowe*, 1993; *Baran and Foot*, 1994]. The observed climatic effects of this particular eruption show substantial warming of the northern hemisphere continents and cooling over the Middle East and Greenland in the winter and subtropical and tropical cooling for about 2 years [*Robock and Mao*, 1995]. Previously, our general circulation model (GCM) study [*Graf et al.*, 1993] suggested that these patterns are all due to the radiative and dynamical responses of the climate system to the volcanic aerosol cloud, but they were idealized experiments conducted in perpetual-January mode with a relatively low resolution model. The mechanism involves warming of the tropical lower stratosphere by volcanic aerosols [*Labitzke et al.*, 1982; *Angell and Korshover*, 1983; *Labitzke and McCormick*, 1992; *Angell*, 1993], an enhanced pole-to-equator temperature gradient producing an enhanced polar vortex, and a wave response in the tropospheric circulation which produces warm advection

[1] Department of Meteorology, University of Maryland, College Park.
[2] Max Planck Institute for Meteorology, Hamburg, Germany.
[3] Now at Department of Environmental Sciences, Rutgers University, New Brunswick, NJ 08901.
[4] Atmospheric, Oceanic and Planetary Physics, University of Oxford, Oxford, England.
[5] Now at Department of Physics and Astronomy, University of Canterbury, Private Bag 4800, Christchurch, New Zealand.
[6] Now at National Center for Atmospheric Research, PO Box 3000 Boulder, CO 80307.
[7] NASA Langley Research Center, Hampton, Virginia.

Paper number 98JD00693.
0148-0227/98/98JD-00693$09.00

anomalies over North America, Europe, and Asia. While we see this dynamical response in both observations [*Kodera*, 1994; *Kodera and Yamazaki*, 1994] and in GCM experiments [*Graf et al.*, 1993], we do not completely understand it. *Perlwitz and Graf* [1995] connect this dynamical effect with linear interaction between stratospheric westerlies and vertically propagating ultralong planetary waves, which is an inherent atmospheric pattern but is enhanced by volcanic forcing. This dynamic response mechanism produces winter warming and is sensitive to model numerics, physical parameterizations, and aerosol parameters. It has not been specifically recognized and discussed in previous GCM simulations [*Hansen et al.*, 1988, 1992; *Pollack et al.*, 1993]. In this work we reexamine this issue with a much improved European Center/Hamburg (ECHAM)4 GCM [*Roeckner et al.*, 1996]. The first step is to assemble an aerosol data set that can be used in a GCM to calculate the radiative perturbation to the climate system. Our preliminary attempts to assemble the necessary data on aerosols and their properties and distributions have shown that even this most recent large eruption was imperfectly observed, and all the data needed to calculate its forcing are not available. We do the best we can, however, by taking advantage of the existing observations. We combine Stratospheric Aerosol and Gas Experiment (SAGE) II aerosol extinctions [*McCormick et al.*, 1995] with Upper Atmosphere Research Satellite (UARS) effective radii [*Lambert et al.*, 1997] to calculate aerosol parameters, as described below, and use stratospheric aerosol measurement (SAM) II, advanced very high resolution radiometer (AVHRR), balloon, and lidar data to support the processing algorithm. This time-dependent zonal-average vertically resolved spectral data set is then used to force a transient ECHAM4 GCM simulation for 2 years after the eruption.

In this paper we describe the assembly of an aerosol data set suitable for GCM experiments. We use this aerosol data set with the ECHAM4 GCM for the post-Pinatubo period with observed and climatological sea surface temperature (SST), as well as with and without the system response to the aerosol radiative forcing. We discuss the definition of the aerosol radiative forcing, the temporal and spatial distribution of the Pinatubo aerosols and the radiative forcing, the contribution of the different spectral bands, the effects of clouds, and the role of climate variability. In a forthcoming paper we shall examine the specific patterns of climate response to this large eruption.

2. Definition of Aerosol Radiative Forcing

Aerosol radiative forcing is a perturbation (calculated as the difference between perturbed and unperturbed values) of atmospheric radiative heating rates and net solar and downward longwave radiative fluxes at the surface caused by aerosols. It could be calculated with atmospheric fields that are not affected by aerosol radiative forcing, or by including the climatic response to the forcing. It is important that both perturbed and unperturbed radiative fluxes or heating rates be calculated on the same atmospheric fields.

There are several definitions of aerosol radiative forcing currently in use. One of the sources of discrepancies in different definitions is in the choice of atmospheric state for the calculations. Another is the location for specification of the radiative perturbations. The Intergovernmental Panel on Climate Change (IPCC) 1995 definition of radiative forcing is the change of net radiation at the tropopause after the stratosphere has reached radiative equilibrium but with no tropospheric response [*Houghton et al.*, 1996, p. 109]. *Dutton et al.* [1992] define aerosol radiative forcing from observations as the difference between the full-spectrum fluxes at the Earth's surface before and after the 1991 Pinatubo eruption, and *Minnis et al.* [1993] define it in the same way but at the top of the atmosphere. *Haywood et al.* [1997] define direct radiative forcing for tropospheric aerosols as the difference in calculated net irradiance at the top of the atmosphere with no atmospheric response. *Lacis et al.* [1992] define radiative forcing in a single column model as the changes of solar fluxes at the tropopause for undisturbed atmospheric temperatures. *Tegen et al.* [1996] calculate the instantaneous radiative forcing of tropospheric dust aerosols in a GCM but with no dynamic effects of the added dust load included.

The IPCC definition [*Houghton et al.*, 1996, p. 109] is useful when comparing radiative forcing from carbon dioxide and other greenhouse gases on a global-average basis, as the climate response is proportional to the strength of the forcing so defined. The IPCC definition, however, mixes the radiative forcing and the response of the climate system. We will evaluate the aerosol radiative forcing here without separate stratospheric equilibration. This definition excludes atmospheric response effects from the forcing but is inconsistent, as discussed below, with forcing estimated from observations.

Volcanic aerosols in the stratosphere heat the stratosphere by absorption of terrestrial longwave radiation and solar near-IR radiation [*Kinne et al.*, 1992]. They also heat both the troposphere and the surface by increasing the downward longwave radiation from the stratospheric aerosol cloud, cool the troposphere (because of reduced absorption by water vapor) by reducing the downward near-IR flux, and cool the surface by reducing both downward visible and near-IR fluxes. The net radiative flux at the tropopause, however, depends on the upward tropospheric longwave flux, which depends on the distributions of clouds, water vapor and surface temperature. All these change when the tropospheric climate changes. Both the stratosphere and troposphere respond dynamically to the radiative perturbations.

Defining the radiative forcing as the change of the net flux at the surface or the tropopause or the top of the atmosphere reflects the change of the total radiative balance of the surface, troposphere or whole atmosphere, but masks the vertical distribution of the heating and its effects on atmospheric processes. As mentioned by *Tegen et al.* [1996] such a definition does not provide sufficient information to fully characterize the effect of aerosols on climate. *Schmitt and Randall* [1991] defined the CO_2 forcing as the initial change in heating rates with no feedback included. In this paper we calculate the atmospheric vertical distribution of heating rates produced by the stratospheric aerosols and the changes of net solar and downward thermal fluxes at the Earth's surface. This set of aerosol radiative forcing parameters is complete, because it is sufficient to force a model which does not include aerosol effects in its radiative code. We can calculate the radiative forcing with any time resolution.

To evaluate whether the state of the climate system or the response of the system affects the radiative forcing, we perform 4 different experiments. Since there was an El Niño during the year after the Pinatubo eruption, we use either the actual SSTs observed during the 2 years after the eruption or climatological SSTs. The different distribution of tropical

cloudiness will produce different upward longwave flux and different stratospheric heating, and we evaluate the magnitude of this effect. We also do the calculations both with and without atmospheric response to the aerosol radiative forcing, evaluating whether the different circulation and resulting distribution of surface temperature, water vapor, and clouds will affect the response to the aerosols. If the change of atmospheric parameters and surface temperature caused by aerosol effects are small enough, the forcing definitions based on different atmospheric states should be close. In these numerical experiments we try to clarify this point.

3. Aerosol Observations

Assessments of the climatic effects of volcanic eruptions suffer from a lack of information about stratospheric aerosol distributions and evolution of their optical characteristics. Observed aerosol extinctions for a few wavelengths or total aerosol optical depth, are not, by themselves, adequate. Although *Sato et al.* [1993] developed a data set of zonally averaged stratospheric aerosol optical depth at $\lambda = 0.55$ μm for the period 1850-1990, construction of spectrally dependent optical depths needs information about aerosol microphysical parameters, because aerosol size distribution and composition define aerosol spectral optical properties. *Lacis et al.* [1992] for the El Chichón case and *Russell et al.* [1993] for the Pinatubo case showed that time variations of the effective radii of bimodal size distributions may significantly change the aerosol radiative forcing integrated over the entire spectrum. In addition, a climate model with a Delta-Eddington-type radiative scheme does not need the total aerosol optical depth but rather the spatial distribution of the aerosol extinction E, single scatter albedo ϖ, and asymmetry parameter g.

Lidar data from a small number of stations [*DeFoor et al.*, 1992; *Winker and Osborne*, 1992; *Avdyushin et al.*, 1993; *Nardi et al.*, 1993; *Jäger et al.*, 1995a, b; *Grant et al.*, 1992; *Ansmann et al.*, 1996; *Di Girolamo et al.*, 1996] which measured the detailed vertical structure of the Pinatubo aerosol are also available, but there are only a few measurements from the latitude of the maximum Pinatubo aerosol concentration (20°S - 20°N), where SAGE II also fails to observe due to saturation in the first months after the eruption [*Veiga*, 1993]. In this context it is important that together with other observations we were able to use a new lidar data set [*Antuña and Sorochinski*, 1994; *Antuña*, 1996] from Camagüey, Cuba.

From May 1991 (1 month before the Pinatubo eruption) until April 1994, balloon-borne measurements of aerosol size distribution were made at Laramie, Wyoming (41.3°N, 105.6°W) by *Deshler et al.* [1992, 1993]. Measurements were conducted once a month, except from June 1991 to May 1992 when they were fortnightly. Measurements were made of temperature, pressure and aerosol concentration from the tropopause to 30 km (approximately from 100 to 10 mbar). The aerosol concentrations were averaged to a 1 km height resolution and their size distributions modeled with either a unimodal or bimodal lognormal distribution. These data were used for calibration of UARS effective radius retrieval (r_{eff}), as well as lidar and other satellite retrievals and in direct study of the aerosol properties [*Jäger et al.*, 1995; *Lambert et al.*, 1996; *Massie et al.*, 1996b].

AVHRR observations of total optical depth [*Stowe*, 1991] and Earth Radiation Budget Experiment (ERBE) radiative balance observations [*Barkstrom*, 1984] are suitable for an independent evaluation of the accuracy of aerosol extinction and radiative forcing. The AVHRR total optical depth itself is not accurate enough, because it incorporates an unknown tropospheric optical depth component, but provides an important upper limit for total aerosol optical depth.

Aerosol size distribution and composition are key factors in the calculation of aerosol spectral optical characteristics, but there are only a few valuable direct measurements of aerosol microphysical structure [*Oberbeck et al.*, 1983; *Hofmann and Rosen*, 1983; *Knollenberg and Huffman*, 1983; *Deshler et al.*, 1992, 1993]. These measurements are conducted only at specific locations and do not provide any horizontal coverage. As a result they contain much structure caused by dynamical and microphysical variability and are not necessarily representative of other locations. There have been several attempts to retrieve aerosol effective radius using spectral measurements from ground-, satellite- or airplane-based instruments [*Thomason*, 1991; *Goodman et al.*, 1994; *Russell et al.*, 1993; *Valero and Pilewskie*, 1992; *Stone et al.*, 1993; *Dutton et al.*, 1994; *Stein et al.*, 1994; *Pueschel et al.*, 1994; *Torres et al.*, 1995; *Rosen et al.*, 1994]. *Lacis et al.* [1996] calculate column average zonal distribution of the effective radius using SAGE II measurements, but the only available latitude- and altitude-dependent effective radius data were retrieved by *Lambert et al.* [1997] from the UARS observations.

The largest time coverage among all global aerosol data with vertical resolution is provided by SAGE II [e.g., *McCormick et al.*, 1979, *Mauldin et al.*, 1985; *McCormick*, 1987; *Thomason*, 1991; *Veiga*, 1993; *Trepte et al.*, 1993]. The observed aerosol extinction is provided at four wavelengths (0.385, 0.453, 0.525, and 1.02 μm) with 5° latitude resolution and vertical resolution of 1 km from an altitude of 5.5 to 40.5 km. The time averaging is irregular, because SAGE II completes one global data collection every 4-6 weeks. Even for a monthly average, there are several periods and locations of missing data, because of collection coverage problems in the midlatitudes and tropics, because no data are collected near the winter poles due to lack of sunlight, and because of saturation in regions of high aerosol optical depth in the lower stratosphere, where the signal drops below the threshold of the instrument [*Veiga*, 1993]. For this study we used the $\lambda = 1.02$ μm data set, which is the most accurate and complete, and is less affected by Rayleigh scattering in the atmosphere than the visible band ($\lambda = 0.525$ μm). One of the authors (LT) processed both the $\lambda = 1.02$ μm and the $\lambda = 0.525$ μm data to fill the holes in midlatitudes and tropics, using lidar data and interpolation along isentropic surfaces [*McCormick et al.*, 1995], and calculated the aerosol optical depth in four layers with boundaries at the tropopause, 20 km, 25 km, 30 km, and the top of the atmosphere, for 10° latitude bands between 75°S and 75°N. SAM II data [*McCormick et al.*, 1979, 1981] are also incomplete but add significant information near the poles. Our analysis of the combined SAM II/SAGE II data set helped to extrapolate aerosol extinction to poles.

The improved stratospheric and mesospheric sounder (ISAMS) [*Lambert et al.* 1996] and the cryogenic limb array etalon spectrometer (CLAES) [*Roche et al.* 1993] carried by UARS include aerosol channels at 12.11 and 12.66 μm,

respectively, and provide better horizontal coverage than SAGE II, but the version of the data used here does not include observations below the 100 mbar level. The ISAMS and CLAES data were used in the periods September 1991 to July 1992, and July 1992 to May 1993. Although the aerosol data are partly contaminated by clouds in the 68-100 mbar layer (especially in the tropics) and the polar data include observations of polar stratospheric clouds, these problems are minor [*Massie et al.*, 1996a; *Lambert et al.*, 1996]. The UARS observations were used to retrieve aerosol volume density and effective radius, which varies with latitude and altitude [*Grainger et al.*, 1995; *Lambert et al.*, 1997]. The UARS retrieval algorithm is calibrated using the *Deshler et al.* [1993] in situ observations. There are some problems with the UARS-retrieved radii: no observations for the first three months after the eruption, relatively poor vertical resolution, small overestimation of r_{eff} above the bulk of the aerosol cloud [*Grainger et al.*, 1995] (although in a region with a small optical depth), and inaccuracy caused by uncertainty of the imaginary part of the refractive index of H_2SO_4 in the LW band.

In this study we used SAGE II aerosol extinctions for 1.02 μm [*McCormick et al.*, 1995] and the effective radii derived from UARS observations [*Grainger et al.*, 1995; *Lambert et al.*, 1997] as the basis for our calculations of a complete set of aerosol parameters over the entire spectrum. The lidar, SAM II, and AVHRR data were used for verification and to estimate aerosol characteristics in the regions with missing data. Using this approach, we developed a spectral aerosol data set for 2 years after the Pinatubo eruption and calculated aerosol radiative forcing with the ECHAM4 GCM.

Sulfate aerosol has a sharp transition from pure scattering in the visible to significant absorption in the near IR (0.68 μm $< \lambda <$ 4 μm) between 2 and 3 μm. The imaginary part of the refractive index of 75% sulfuric acid increases by 2 orders of magnitude in this interval from 10^{-3} to 10^{-1}. The shape of this transformation is sensitive to the aerosol size distribution and significantly affects the amount of solar energy which can be absorbed. In contrast with the opinion that LW aerosol heating dominates everywhere in the stratosphere [*Kinne et al.*, 1992], we found that in our earlier calculations aerosol absorption in the near IR produces important heating effects [*Stenchikov and Robock*, 1994] at altitudes higher than those where LW heating dominates. Here we show that vertical variation of the effective radius is very important, and small particles at the top of the aerosol cloud cause a significant near-IR stratospheric heating.

Kinne et al. [1992] used a bimodal lognormal aerosol size distribution with column average parameters. *Shibata et al.* [1996] combined SAGE II observations and an aerosol lognormal size distribution with a fixed median radius of 0.6 μm to estimate the aerosol radiative effect on stratosphere. *Lacis et al.* [1996] derived column-averaged r_{eff} from SAGE II spectral optical depths by searching for a least squares best fit of a unimodal lognormal size distribution. Because of simplified assumptions about the distribution of the aerosol characteristics, none of these studies revealed significant near-IR heating at the top of the aerosol cloud. *Eluszkiewicz et al.* [1996] calculated forcing only for four different aerosol profiles in the tropics and midlatitudes. They retrieved both effective radius and particle density from ISAMS LW measurements and got a maximum solar heating rate of only about 0.1 K/d. This is because they probably underestimate the number of small particles, due to using only LW observations. LW radiative effects are not sensitive to the number of small particles.

4. Aerosol Data Set for GCM Experiments

The observed aerosol cloud took on a zonal structure within a few weeks after the eruption and changed smoothly in time [*McCormick et al.*, 1995]. Therefore we chose to produce a data set with zonal mean aerosol parameters and a 1 month time step. This level of accuracy is appropriate for the physical problem and the available observations.

As the basis for our aerosol calculations, we use the SAGE II optical depth $\tau(z,\varphi,t)$ for four layers in the lower stratosphere: tropopause to 20 km, 20 to 25 km, 25 to 30 km, and above 30 km, for λ = 1.02 μm and UARS-retrieved effective radius $r_{eff}(p,\varphi,t)$ [*Lambert et al.*, 1997]. (The optical depths for λ = 0.525 μm from SAGE II have lower accuracy and are used only for verification purposes.) The input fields $\tau(z,\varphi,t)$ and $r_{eff}(p,\varphi,t)$ characterize the aerosol particle density, size distribution, and refractive index. They depend on altitude z or pressure p, latitude φ, and time t and are provided on different space-time grids. The processing is split into two main steps. First, we fill the data gaps and interpolate the input fields in space and time to the target grid, and then we calculate aerosol spectral optical characteristics using the Mie theory package [*Wiscombe*, 1980]. The set of output fields includes the aerosol extinction $E(p,\varphi,\lambda,t)$, the single-scatter albedo $\varpi(p,\varphi,\lambda,t)$, and the asymmetry parameter $g(p,\varphi,\lambda,t)$ on a space-time grid suitable for model calculations. We discuss the processing algorithm in more detail below.

4.1. Space-Time Distribution

In this study we develop the data set for the particular case of the ECHAM4/T42 19 layer spectral model [*Roeckner et al.*, 1996], which uses the same spatial grid as the previous ECHAM3 model [*Deutsches Klimarechenzentrum*, 1993], and present our results for this particular case. ECHAM4 is very successful in reproducing the observed climate in the Atmospheric Model Intercomparison Project (AMIP) [*Stendel and Bengtsson*, 1997]. The ECHAM4 calculations are performed on a 64 node Gaussian latitude grid. The vertical coordinate is a hybrid pressure coordinate, which coincides with sigma coordinates near the surface and transforms into pressure coordinates in the stratosphere [*Deutsches Klimarechenzentrum*, 1993].

To interpolate from a particular altitude to the ECHAM4 hybrid pressure vertical grid, we calculated the altitudes of the hybrid pressure levels using consistent meteorological parameters from the ECHAM4 AMIP run for the period of the investigation. The tropopause is approximated by the 200 mbar pressure surface and the top of the aerosol cloud by the 2.24 mbar level, which corresponds to an altitude of approximately 40 km. The results are not sensitive to these approximations, because virtually the entire mass of the aerosol cloud is in the layer below 10 mbar and above 100 mbar. SAGE II does not provide aerosol extinction near the poles; therefore we extrapolate the value from the closest grid point along isobars. In those cases where SAM II aerosol extinctions are available and cover regions closer to poles than SAGE II, the comparison shows that this algorithm works reasonably well. We did not spread SAGE II data into the troposphere below 200 mbar. Below the tropopause, efficient

deposition processes rapidly remove volcanic aerosols from the troposphere. The lidar soundings confirm that the main part of aerosol cloud is above this level [*DeFoor et al.*, 1992; *Winker and Osborne*, 1992; *Avdyushin et al.*, 1993; *Nardi et al.*, 1993; *Jäger et al.*, 1995a, 1995b; *Grant et al.*, 1992; *Ansmann et al.*, 1996; *Di Girolamo et al.*, 1996]. Figure 1 demonstrates this vertical structure of the aerosol distribution measured at Camagüey, Cuba (21.2°N). at the northern edge of the dense core of the volcanic cloud [*Antuña and Sorochinski* , 1994].

The UARS effective radii were extrapolated to the poles (along pressure surfaces) and down below 100 mbar (where there are no data) by applying the last available value in latitude or altitude, respectively. *Deshler et al.*'s [1993] data set shows that the size distribution does not change dramatically below 100 mbar, and since the greater part of the aerosol cloud is located higher than 100 mbar most of the time, this extrapolation does not introduce significant errors. We also use September data for the initial stage after the eruption, because UARS observations are not available until September 1991. This is potentially more uncertain, because in the initial stage, the effective radius grows from a pre-Pinatubo level of $r_{\text{eff}} \approx 0.17$-$0.19$ μm [*Russell et al.*, 1996] before the eruption to $r_{\text{eff}} \approx 0.5$-$0.6$ μm for the well-developed volcanic aerosol cloud. We could interpolate an r_{eff} between these two values, but the fresh Pinatubo aerosol just after eruption has very separated small and large modes. The effective radius is a very poor and inaccurate characteristic of such a distribution anyway. Therefore we decided not to include additional assumptions and use the closest retrieved values, until additional information becomes available.

Volcanic ash, before it falls out of the atmosphere, provides an additional source of uncertainty at the initial stage of development of the volcanic cloud, the first 1-2 months after the eruption. Because of a different refractive index (it absorbs much more of solar radiation than sulfate aerosol), complex shape, and unknown number-size distribution, the radiative effects are different from sulfate aerosols. Although the first 2 months after the eruption are characterized by dramatic changes of microphysical and optical properties of the aerosol cloud, this initial stage is short enough to not produce a long-term climatic signal.

4.2. Aerosol Spectral Characteristics

To conduct radiative calculations in a GCM, we must provide aerosol optical characteristics for the entire spectrum with the specific resolution used in a particular model. Since the ECHAM4 radiative transport code uses broadband spectral intervals, we need to average the aerosol characteristics over wavelength.

The radiation scheme of ECHAM4 has been adopted from the European Center for Medium-Range Weather Forecasting (ECMWF) model [*Fouquart and Bonnel*, 1980; *Morcrette et al.*, 1986]. The descriptions of greenhouse gas absorption and water vapor continuum effects have been improved [*Giorgetta*

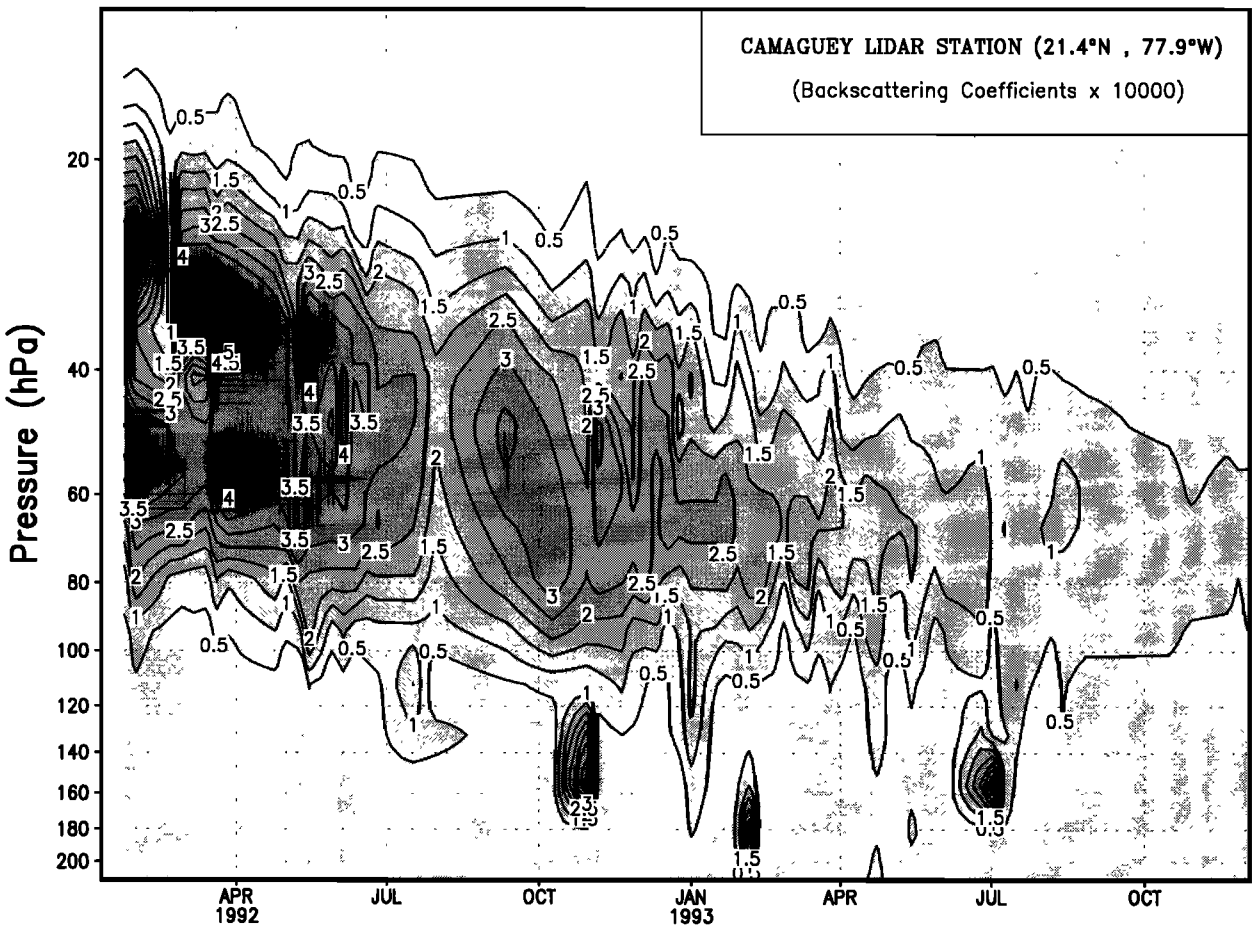

Figure 1. Aerosol backscattering coefficient at $\lambda = 0.532$ μm as a function of pressure and time derived from lidar measurements taken at Camagüey, Cuba (21.2°N), for the period January 1992 to November 1993.

and Wild, 1995], optical properties of clouds have been parameterized in terms of liquid and ice water content [*Roeckner*, 1995], and aerosol effects are included for the first time. It is a broadband model with two spectral intervals in the solar (visible: 0.25 μm < λ < 0.68 μm; near IR: 0.68 μm < λ < 4 μm), and seven basic intervals in the LW. After combination of two basic water vapor intervals into one combined interval as well as two basic intervals for the atmospheric window, the model altogether operates with seven combined spectral intervals in the range of wavelength 0.25 μm < λ < 250 μm: 0.25-0.68 μm, 0.68-4 μm, 3.56-8.0 μm combined with 28.6-250 μm, 12.5-20.0 μm, 8.0-9.0 μm combined with 10.3-12.5 μm, 9.0-10.3 μm, and 20.0-28.6 μm [*Morcrette et al.*, 1986].

To conduct Mie calculations of aerosol optical and LW characteristics, we need to know the aerosol density, size distribution, and aerosol chemical composition, which defines the refractive index of the aerosol particles. Volcanic aerosol particles are mostly spherical droplets of sulfuric acid solution. The concentration of the solution depends on temperature and humidity, can vary from 70% to 80% for the midlatitudes and tropics, and decreases to 40-50% near the winter poles due to low temperatures [*Yue et al.*, 1994; *Russell et al.*, 1996; *Lambert et al.*, 1997]. The refractive index has a weak temperature dependence. The refractive index of sulfuric acid has been measured for different concentrations by *Palmer and Williams* [1975] and for 75% and 90% solutions in the LW bands by *Remsberg et al.* [1974] at room temperature. The imaginary part of the refractive index in the LW for these two observations differs by up to 50%, which causes problems for CLAES/ISAMS retrieval [*Grainger et al.*, 1995]. Because of discrepancies in the observations and insufficient information about aerosol chemical composition and temperature, we did not try to be very precise with this parameter and use the refractive index for a 75% solution of sulfuric acid [*Palmer and Williams*, 1975], which is roughly appropriate for all cases. We calculate the aerosol optical characteristics in the Mie approximation assuming a unimodal lognormal aerosol size distribution $n(r)$ [*Davies*, 1974]:

$$n(r) = \frac{1}{r}\frac{N}{\sqrt{2\pi}\ln\sigma}\exp\left[-\frac{(\ln r-\ln r_o)^2}{2(\ln\sigma)^2}\right]\left[\frac{\text{number}}{\text{cm}^3\,\mu\text{m}}\right] \quad (1)$$

where r is the aerosol radius, σ characterizes the width of the size distribution, r_o is the median radius, and $N(p,\varphi,t)$ is the aerosol particle density. *Grainger et al.* [1995] retrieved effective radius and aerosol volume density using UARS measurements and in situ balloon observations by *Deshler et al.* [1993]. Here we use only UARS-retrieved effective radius and calculate the aerosol density using SAGE II extinctions for 1.02 μm. Then, assuming that σ is fixed in time and space (because there is no strong dependence on this parameter), we choose its value to get a best fit of calculated and UARS-retrieved optical depth for 12.66 μm.

The median radius is determined from the UARS-retrieved effective radius $r_{eff}(p,\varphi,t)$:

$$r_o = r_{\text{eff}}\exp\left[-2.5(\ln\sigma)^2\right] \quad (2)$$

It is well known [*Pueschel et al.*, 1992] that the volcanically enhanced aerosol distribution is often bimodal, as measured by *Deshler et al.* [1993]. The accuracy of the unimodal distribution (1) in comparison with the bimodal distribution has been studied by *Russell et al.* [1996], who showed that for modes that overlap, the unimodal distribution provides an accurate enough approximation compared to the other uncertainties.

The aerosol extinction E (m^{-1}) for a particular wavelength is proportional to the number of aerosol particles N in a unit volume:

$$E(\lambda) = \int Q_{\text{ext}}\left(\frac{2\pi r}{\lambda}, m(\lambda)\right)\pi r^2 n(r)dr \times 10^{-6} \quad (3)$$

Q_{ext} is a dimensionless Mie efficiency factor of refraction which depends on the complex index of refraction $m(\lambda)$, wavelength λ (μm), and particle radius r (μm).

Therefore first we calculate the aerosol extinction $E_1(p,\varphi,\lambda=1.02\ \mu m,t)$ assuming $N = 1$ in (1) with some initial width σ and define the density $N(p,\varphi,t)$ of aerosols as the ratio of the calculated aerosol extinction and the observed SAGE II extinction $E_S(p,\varphi,\lambda=1.02\ \mu m,t)$:

$$N(p,\varphi,t) = \frac{E_S(p,\varphi,\lambda = 1.02\ \mu m,t)}{E_1(p,\varphi,\lambda = 1.02\ \mu m,t)} \quad (4)$$

$N(p,\varphi,t)$ calculated from (4) is of the order of 10 cm^{-3}, which is in a good agreement with direct number/size distribution observations [*Deshler et al.*, 1992, 1993]. With this $N(p,\varphi,t)$ we calculate the aerosol optical parameters in the Mie approximation [*Wiscombe*, 1980] for all wavelengths assuming size distribution (1). For λ = 1.02 μm, the calculated aerosol extinction always automatically equals the SAGE II observed extinction:

$$E(p,\varphi,\lambda=1.02\ \mu m,t) = E_S(p,\varphi,\lambda=1.02\ \mu m,t).$$

We then repeat these calculations changing σ in (1) and (2) to get a better agreement with the observed CLAES/ISAMS LW optical depths for 12.66 μm. The time evolution of aerosol extinctions and effective radius are shown in Figure 2. Figure 3 shows the calculated total optical depth in the visible (λ = 0.525 μm), near IR (λ = 1.02 μm), and LW (λ = 12.66 μm) wavelengths. We demonstrate results in the visible for the widely used wavelength of 0.55 μm but do comparisons with the SAGE II observations for its wavelength of 0.525 μm.

We start our iterations with σ = 2 and obtain the best fit of the calculated optical depth in the LW to the CLAES optical depths for σ = 1.25. Figures 3c and 3f show that the calculated optical depth for λ = 12.66 μm agrees quite well with the CLAES total optical depth. *Lacis et al.* [1992] showed that aerosol radiative forcing at the tropopause depends primarily on r_{eff} and not on σ and that the dependence on σ is relatively significant only for r_{eff} = 0.4-0.8 μm. The observed UARS effective radii, however, are exactly in this range! As a result, our fitting of the standard deviation causes a 20% increase of 0.55 μm extinction. In calculations with different σ the extinction for 1.02 μm is fixed at the observed level. The value of σ obtained (1.25) is relatively small, but

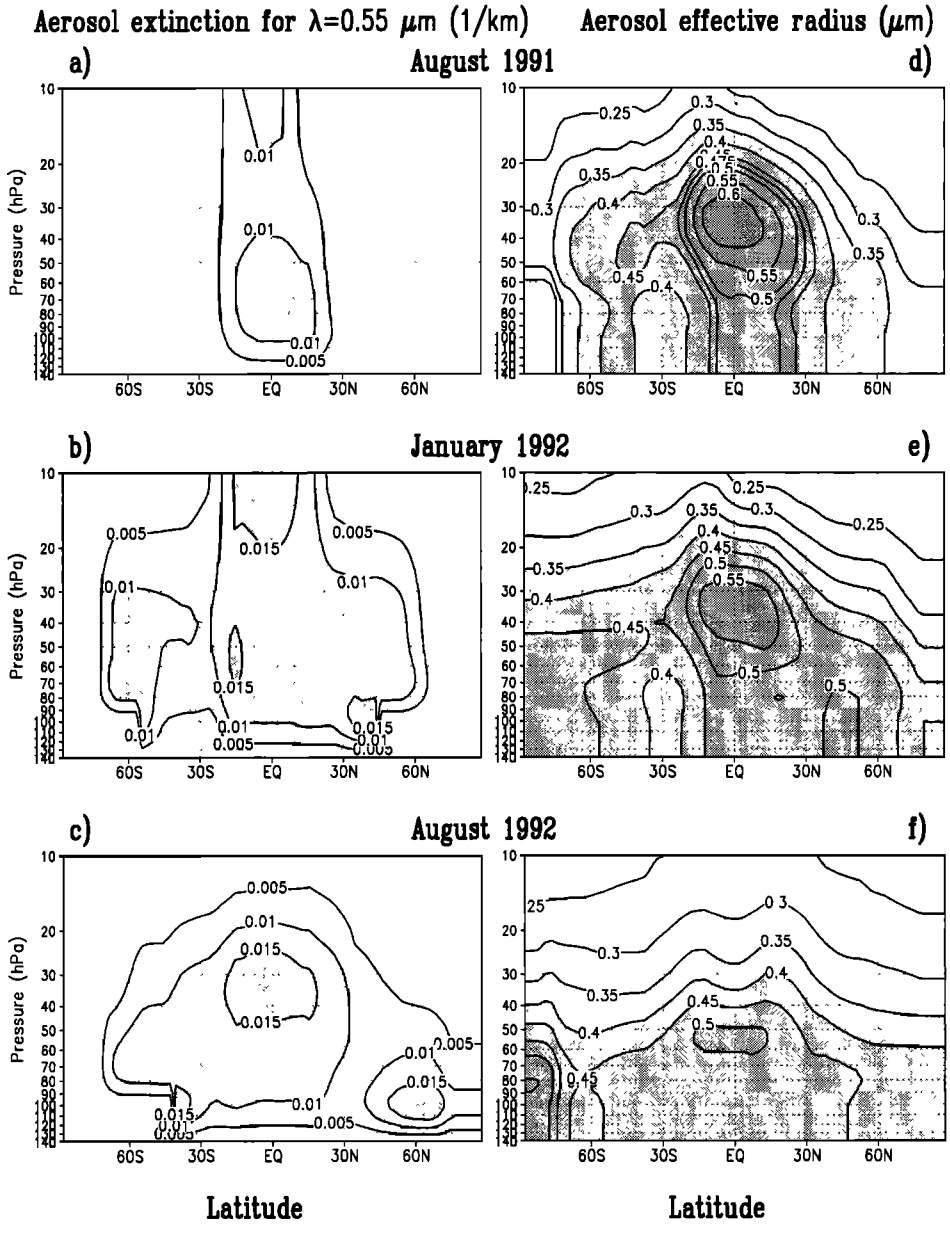

Figure 2. Zonal mean cross sections of aerosol extinction (1/km) in the visible (λ = 0.55 μm) and effective radius (μm) for August 1991, January 1992, and August 1992.

reasonable, because it corresponds to the width of the distribution of the large mode in the two mode distributions observed by *Deshler et al.* [1995]. The obtained value of σ could be affected by the assumption about its independence on time and space. Calculation of the width of the distribution at each point, however, would give unstable results, because of the weak dependence of aerosol radiative properties on σ.

We use a nonuniform grid in spectral space with 60 spectral intervals and calculate aerosol optical characteristics with relatively high resolution at wavelengths in the regions of sharp changes of aerosol parameters. Then we average the aerosol optical characteristics at each grid point to the broadband intervals of the ECHAM4 radiative scheme [*Fouquart and Bonnel*, 1980; *Morcrette*, 1984; *Morcrette and Fouquart*, 1985; *Morcrette et al.*, 1986] using the Planck function $B(\lambda,T)$ for T = 6000 K and T = 300 K as the weighting for integration of the parameters in the solar and LW bands, respectively. The averaging procedure is similar to one described by *d'Almeida et al.* [1991]:

$$\overline{E(\lambda)} = \int_a^b E(\lambda)B(\lambda,T)d\lambda \Big/ \int_a^b B(\lambda,T)d\lambda$$

$$\overline{\varpi(\lambda)} = \int_a^b \varpi(\lambda)E(\lambda)B(\lambda,T)d\lambda \Big/ \int_a^b E(\lambda)B(\lambda,T)d\lambda \qquad (5)$$

$$\overline{g(\lambda)} = \int_a^b g(\lambda)\varpi(\lambda)E(\lambda)B(\lambda,T)d\lambda \Big/ \int_a^b \varpi(\lambda)E(\lambda)B(\lambda,T)d\lambda$$

where a and b are the boundaries of the particular broadband spectral interval.

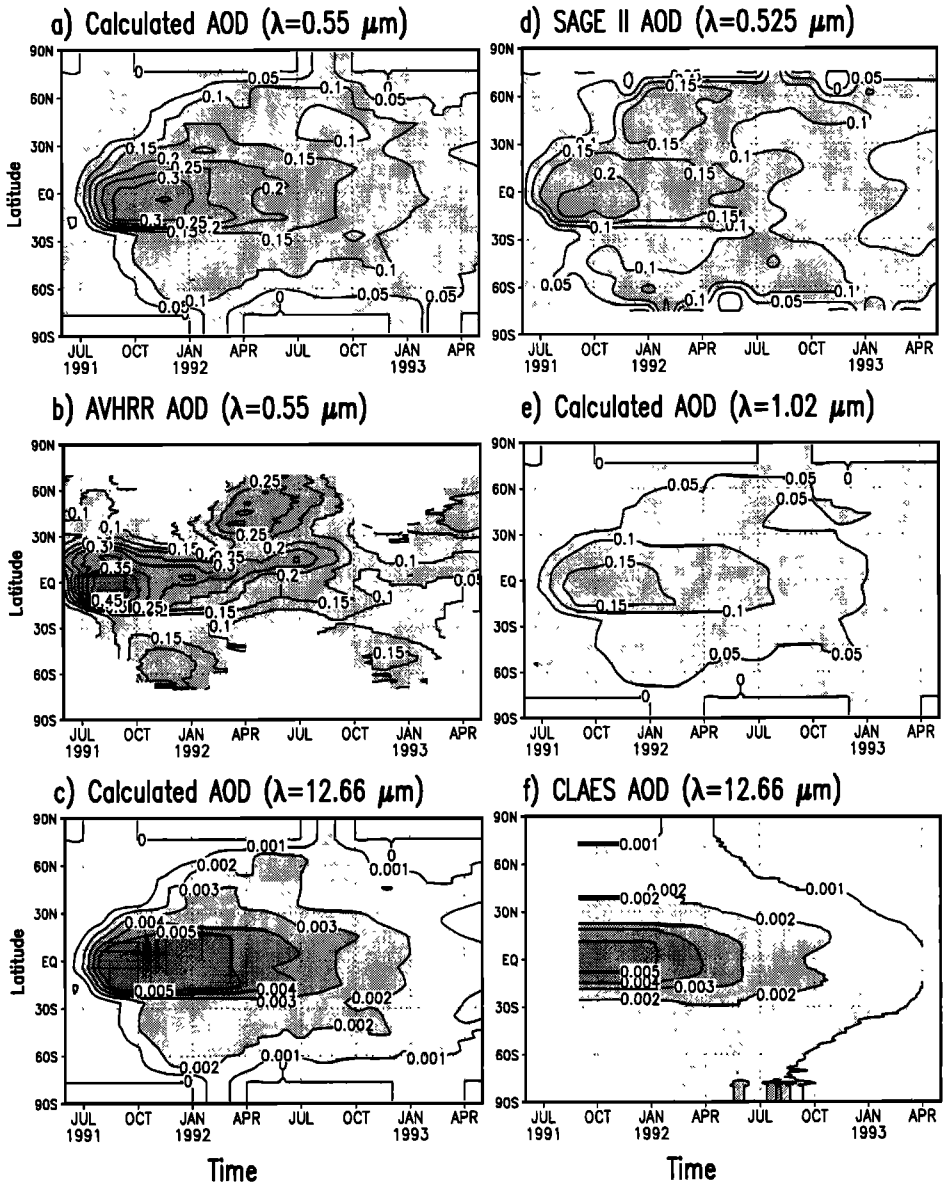

Figure 3. Calculated optical depth for (a) λ = 0.55 μm, (c) λ = 12.66 μm, and (e) λ = 1.02 μm, and observed (b) AVHRR total optical depth for λ = 0.25 μm, (d) SAGE II total optical depth for λ = 0.525 μm and (f) CLAES total optical depth for λ = 12.66 μm.

4.3. Aerosol Data Set

After injection of sulfur dioxide gas into the stratosphere by the eruption, the aerosol extinction increases for almost half a year and spreads to the poles (Figures 2, 3). Transport in the meridional circulation cells and seasonal penetration to the poles are clearly seen in Figures 3a-3c. The maximum extinction is first located at the 50-80 mbar layer in August 1991. In January 1992 there are several regions of maximum extinction at high levels in the tropics and in lower levels in midlatitudes. Later in August 1992 the core of the aerosol cloud shifts in the tropics to 30-50 mbar and goes down to 100 mbar in the midlatitudes. The largest particles, with r_{eff} = 0.5 μm, are located mostly in the tropical core of the cloud (Figures 2d-2f). They slowly fall down from the 30-40 mbar level in August 1991 to 60 mbar in August 1992. The maximum total optical depth in the visible reaches 0.35 in October and November 1991 (Figure 3a).

The nonuniform spatial distribution of the effective radius significantly affects the aerosol optics. The shifting of the visible extinction maximum upward in the tropics in comparison with the near IR [*Trepte et al.*, 1993] is entirely due to the selective influence of size distribution on the aerosol optical properties for different wavelengths. The particles in the 10-20 mbar layer (r_{eff} = 0.25-0.3 μm) have half the effective radius of the core of the cloud, where effective radius reaches 0.55-0.60 μm. The small particles are more effective in scattering the visible radiation (λ = 0.55 μm) than the near IR (λ = 1.02 μm). As a result, the same amount of small particles which produces the observed aerosol extinction at λ = 1.02 μm produces a larger extinction in the visible and shifts the maximum extinction for λ = 0.55 μm to the 10-20 mbar layer (Figures 2a-2c). The near-IR extinction for λ = 1.02 μm has a maximum significantly lower at 40-50 mbar [*Trepte et al.*, 1993].

For $\lambda = 0.525$ μm, the total calculated aerosol optical depth is larger than that observed by SAGE II over the equatorial region (Figures 3a, 3d). It reaches a maximum value of 0.35, which is a little less than the slightly overestimated AVHRR optical depth [*Long and Stowe*, 1994] shown in Figure 3b but is in a good agreement with the automatic precision sunphotometer spectral measurements at Mauna Loa [*Dutton et al.*, 1994]. The SAGE II total optical depth in the visible (Figure 3d) for the latitude of Mauna Loa is much less than that discussed by *Dutton et al.* [1994] and only half of the maximum AVHRR optical depth (Figure 3b); therefore in this case the suspicion about the effect of supersaturating is still relevant. In the tropics the total calculated aerosol optical depth in the visible is approximately twice that in the near IR at $\lambda = 1.02$ μm during half a year after the eruption and then decreases and becomes closer to the near-IR optical depth. This demonstrates the flattening of the aerosol spectral extinction, as discussed by *Russell et al.* [1996]. The SAGE II optical depth in the visible is practically the same as in the near IR during the first half year after eruption. This discrepancy might be connected with the severe problem of reconstruction of the aerosol parameters in the regions of saturation in the visible in the lower part of the cloud in the tropics.

The flattening of the total aerosol spectral optical depth distribution during the first few months after the eruption observed by *Dutton et al.* [1994] is an important feature of the evolution of the aerosol optical properties. This feature is directly connected to aerosol microphysical transformations and changes of the effective radius [*Russell et al.*, 1996]. In our case, the effective radius depends on altitude, latitude, and time. To get a column average effective radius [$\overline{r_{\text{eff}}(\varphi,t)}$], which characterizes the spectral behavior of the aerosol optical depth, we must account for the number of particles at different altitudes $N(p,\varphi,t)$ with different effective radii. Because we assumed that σ does not depend on altitude, we can use the simple relation:

$$\overline{r_{\text{eff}}(\varphi,t)} = \frac{\int_{p=10\text{mbar}}^{p=200\text{mbar}} N(p,\varphi,t)\, r_{\text{eff}}^3(p,\varphi,t)\, dp}{\int_{p=10\text{mbar}}^{p=200\text{mbar}} N(p,\varphi,t)\, r_{\text{eff}}^2(p,\varphi,t)\, dp}$$

The column average effective radius is shown in Figure 4 for 7°S and 40°N. It combines both particle density, calculated from SAGE II extinctions, and effective radii, calculated for different altitudes from ISAMS measurements. Although the effective radius from *Grainger et al.* [1995] decreases monotonically in time, the column average effective radius is non monotonic [*Russell et al.*, 1996]. Just after the eruption, $\overline{r_{\text{eff}}(\varphi,t)}$ increases in the equatorial region, probably because of the effect of large ash particles, and then decreases by October-November 1991 to a value that is still twice the pre-eruption one (0.17-0.19 μm [*Russell et al.*, 1996]). After that, the effective radius increases due to aggregation of the particles both in the tropics and in the midlatitudes during the year after the eruption in accordance with the observations collected by *Russell et al.* [1996], and this causes the flattening of the optical depth spectrum. Our maximum value of the effective radius is slightly less than in the work of *Russell et al.* [1996]. Therefore in our case, the maximum optical depth is in the visible part of spectrum and not in the near IR, as discussed by *Russell et al.* [1996]. These calculations show that combination of two different independent sources of satellite data can provide a very reasonable picture of the

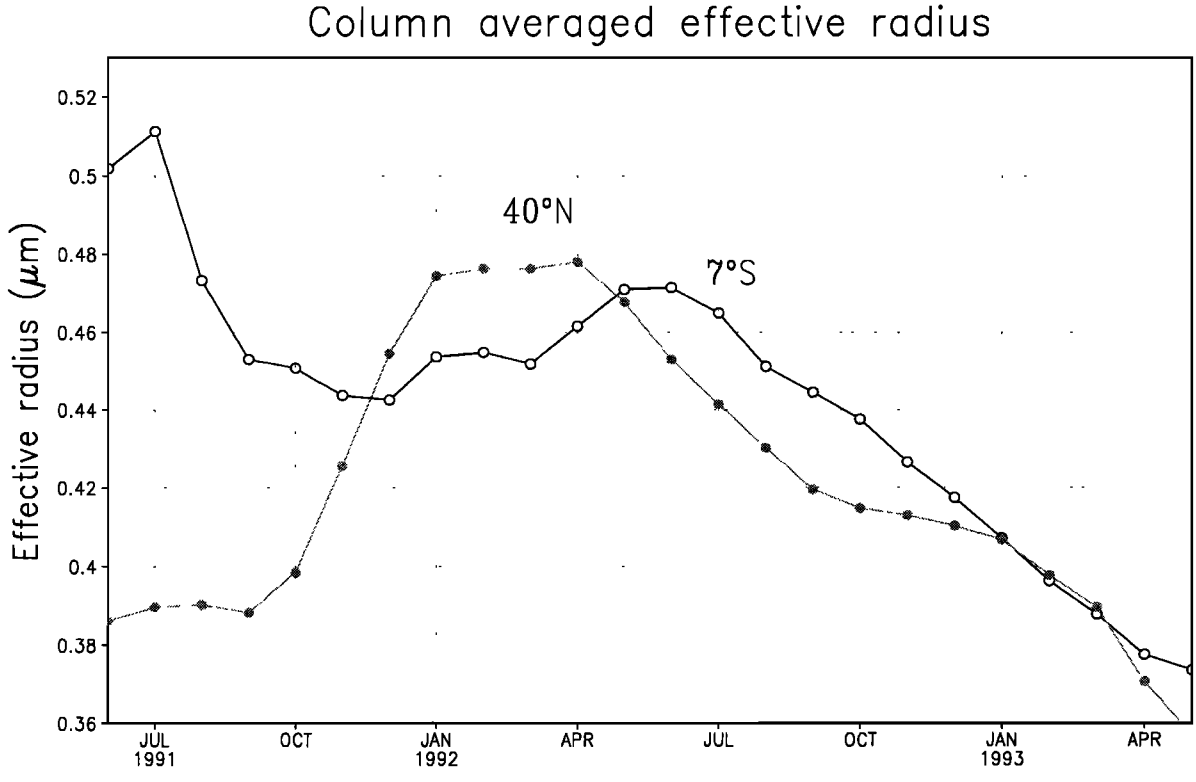

Figure 4. Column averaged aerosol effective radius (μm) for 7°S and 40°N.

evolution of the aerosol microphysical parameters even when each source is not absolutely perfect.

Figures 3c and 3f show that the calculated optical depth for λ=12.66 μm is close to the one observed by the CLAES instrument aboard UARS. The total aerosol optical depth in the visible is almost 2 orders of magnitude larger than in the LW (Figures 3a, 3b). Sulfate aerosol, however, is purely scattering in the visible (ϖ = 1) and does not heat the atmosphere by absorption in the visible solar bands. In the LW, ϖ is close to zero and aerosol absorption of terrestrial radiation produces significant stratospheric heating even with 2 orders smaller optical depth than in the visible. *Kinne et al.* [1992] are of the opinion that this is the most significant source of stratospheric heating caused by sulfate aerosol. Our calculations show that in the near IR, where the optical depth is substantially less than in the visible, almost 10% of solar radiation at $\lambda \cong 2.5$ μm is absorbed. The single-scattering albedo of sulfate aerosols decreases sharply only at $\lambda_a \cong 2.5$ μm. The solar flux in this band $\lambda_a < \lambda < 4$ μm, where aerosol absorption is significant, is much less than in the entire near-IR band and is very sensitive to the actual value of λ_a. Therefore we pay particular attention to accurately calculate, with high spectral resolution, the sharp transition from scattering to absorption in the near IR to account for this solar heating. We also found that variation of the effective radius with altitude may be of great importance, because of stronger absorption of near-IR radiation by the small (in comparison with the wavelength) particles.

5. Radiative Forcing by the Aerosol Cloud

To calculate aerosol radiative forcing, we perform four 2-year simulations with the ECHAM4 GCM for the Pinatubo period, for June 1991 through May 1993, using initial conditions from the ECHAM4 AMIP runs [*Stendel and Bengtsson*, 1997]. (Although we discuss here a particular GCM, we can calculate aerosol parameters for any spatial and spectral resolution.) As shown in Table 1, we used either observed (O) or climatological (C) SSTs and performed the calculations either with (AC and AO) or without (C and O) accounting for the effects of radiative forcing from the specified distribution and optical properties of the Pinatubo aerosols on atmospheric dynamics. In all four simulations, however, we calculated the radiative heating rates and fluxes for two cases, with and without stratospheric aerosols, whether the climate system was allowed to respond or not. Thus by comparing the two cases (for each experiment in Table 1), we can calculate the radiative forcing and examine the dependence of the radiative forcing on the method of the calculation. Each calculation of heating rates and fluxes is also performed for clear-sky conditions, in which the effects of simulated clouds are ignored, so that the effects of clouds on the forcing can be investigated.

We know that for GCM simulations of the climatic response to a particular forcing, it is necessary to perform ensemble calculations, and for our investigations of the climatic response, we performed an ensemble of five different realizations for each of the four simulations in Table 1. For the purposes of this paper, however, the results (discussed below) are so definitive that ensembles are not necessary.

In this section we discuss the results of our forcing calculations first looking at the spatial distribution of the flux perturbations for different wave bands. We compare all-sky and clear-sky cases, and separate physical and model-related effects. Next, we analyze the space/time structure of the zonal-mean, aerosol-induced change of radiative heating rates and fluxes and reveal the role of different effects.

5.1. Horizontal and Vertical Structure of Radiative Forcing

The geographic distribution of the changes of all-sky monthly mean radiative fluxes caused by aerosols, at the top of the atmosphere, at the tropopause, and at the Earth's surface in the visible (0.2-0.68 μm), near IR (0.68-4 μm), LW (4-250 μm), and total (integrated over the entire spectrum) for January 1992 for the C case are shown in Figures 5 and 6. For both solar and LW we define the downward flux as positive and the upward as negative. This means that a positive perturbation of any flux (solar or LW) heats the system, but a negative one cools it. Both solar fluxes (visible and near-IR) decrease at all levels. The visible radiation is not absorbed by aerosols and clouds but only reflected, and therefore the changes of net flux are virtually the same at all the levels. The near-IR radiation is well absorbed by clouds and water vapor and slightly absorbed by the aerosols. Both of the flux perturbations (Figure 5) are not zonal, because of the interactions with cloudiness and the nonzonal distribution of surface albedo and atmospheric water vapor. The perturbation in the visible flux has the strongest value of -4 to -5 W/m^2. The near-IR flux perturbation, compared to the visible, is stronger at the tropopause (up to -6 to -7 W/m^2), the same as the visible at the top of the atmosphere (-4 to -5 W/m^2), and weaker than the visible at the surface (-3 to -4 W/m^2). The dense clouds in the tropics damp the visible perturbations at all levels because of reflection. The near-IR flux is absorbed by the clouds and tropospheric water vapor; therefore the near-IR forcing is significantly weaker at the surface.

Table 1. Labels for General Circulation Model Runs Based on Boundary Conditions

	Climatological SST	Observed SST (El Niño)
No aerosol forcing	C	O
With Aerosol forcing	AC	AO

SST, Sea surface temperature.

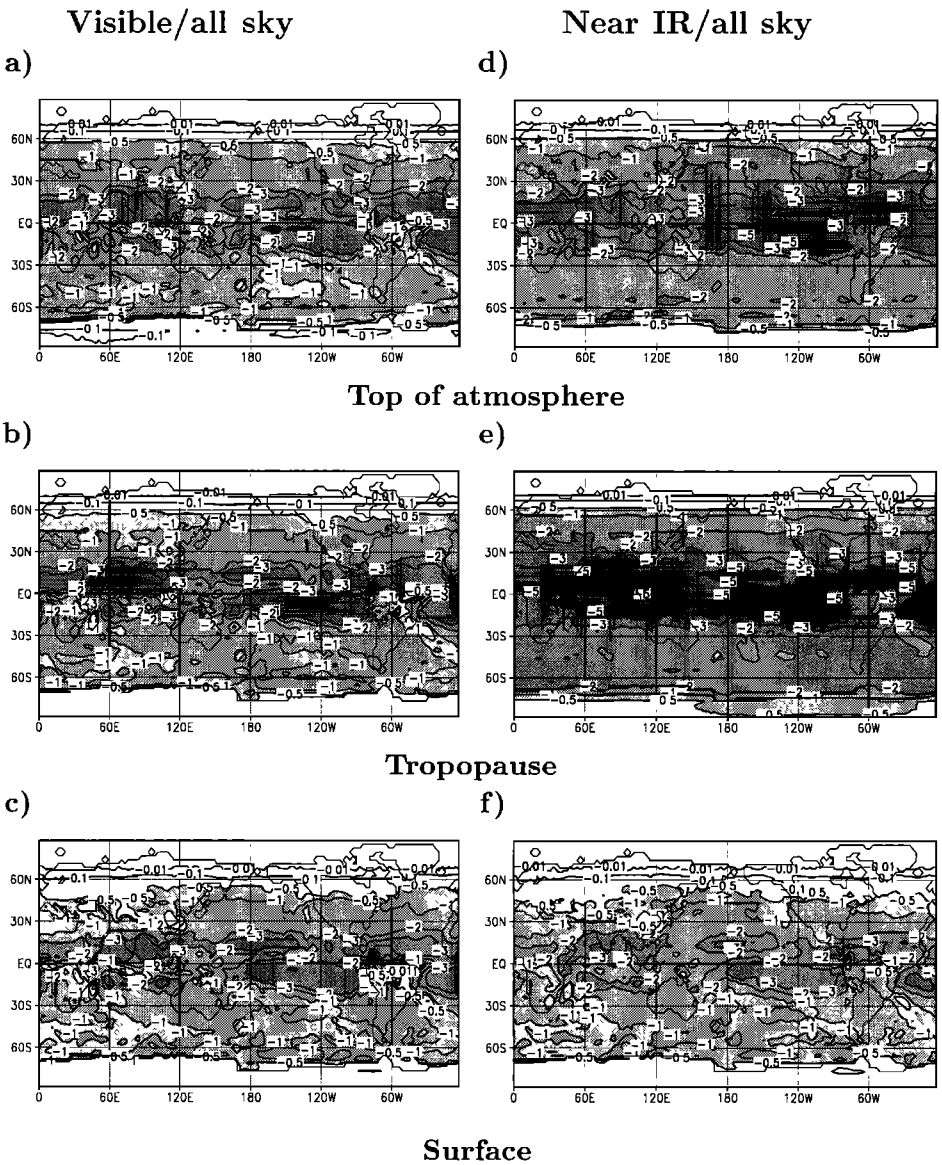

Figure 5. Geographic distribution of monthly averaged changes of all-sky visible (integrated over the 0.2-0.68 μm spectral band) radiative net flux (W/m^2) for January 1992 caused by aerosols in run C (climatological SST/no aerosol response) (a) at the top of atmosphere, (b) the tropopause, and (c) the surface and the same for the near IR (integrated over the 0.68-4 μm spectral band) at (d) the top, (e) tropopause, and (f) surface.

The LW flux perturbation at the tropopause (Figure 6b), which is caused by aerosol thermal irradiation, is practically zonal, because it is defined by the stratospheric temperature and the aerosol optical depth, which both are almost zonal. The heating of the troposphere caused by LW forcing reaches 2-3 W/m^2 (Figure 6b). The LW perturbations at the top and at the surface (Figures 6a, 6c) are affected by clouds and the inhomogeneity of the tropospheric properties. The aerosols absorb up to 3-4 W/m^2 from the outgoing thermal flux. The atmospheric and cloud absorption substantially decrease the LW perturbations at the surface, where it reaches only 0.5 W/m^2.

The total (visible + near-IR + LW) flux perturbation is mainly negative, except in the winter pole region, where there is no solar radiation but only LW (Figures 6d-6f). The maximum total flux perturbation is stronger than -7 W/m^2. There are small spots with slightly positive forcing at the top, which are caused by strong cloud reflection and, as a result, weakening of the negative solar forcing and prevailing of positive LW forcing. In other seasons we observed such weakening of the solar forcing over the Sahara, because of large surface reflection amplified by the background tropospheric aerosol. The Morcrette scheme accounts for multiple reflection between the aerosol layer and the underlying reflective surface (cloud top or land surface with high albedo). It probably overestimates the weakening of solar forcing because of the above effect, in comparison with control calculations we performed with two other models [*Chou*, 1992; *Frolkis and Rozanov*, 1992].

It is interesting to compare the all-sky flux perturbations in Figures 5c, 5f, and 6c-f with the clear-sky perturbations shown in Figure 7. Global and regional clear-sky values are

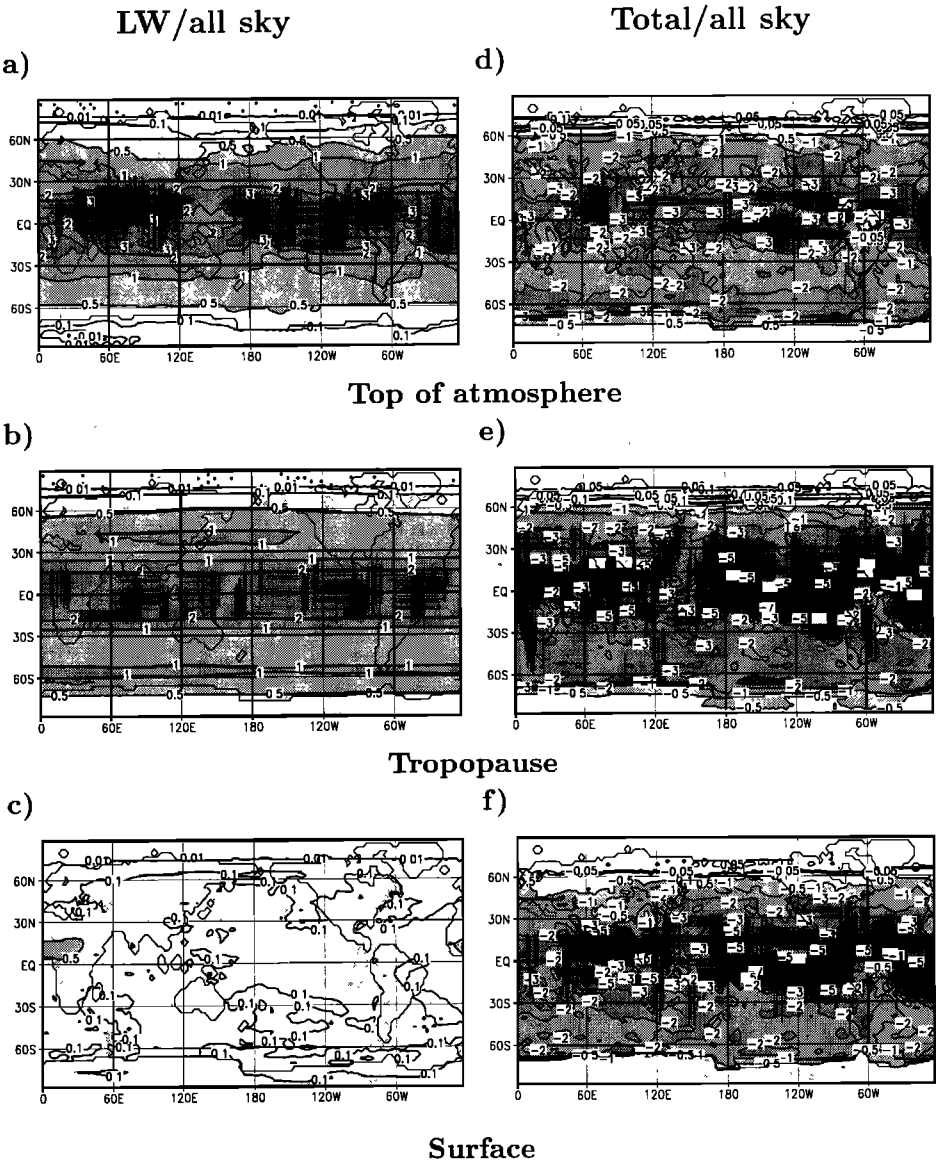

Figure 6. Same as Figure 5 for all-sky LW (integrated over the 4-250 μm spectral band) radiative net flux (W/m^2) and for the total (integrated over the 0.2-250 μm spectral band) net flux.

20-40% larger. The LW perturbation at the surface is affected by the non-uniform distribution of atmospheric water vapor and does not look zonal. The solar perturbations are much more zonal than for the all-sky case. This confirms that clouds modify the solar forcing significantly and provide a strong non-zonal signal.

5.2 Spurious Systematic Error in Clear-Sky Solar Component of Radiative Forcing

Both the clear-sky-solar perturbations (visible and near-IR) are contaminated by a periodic noise (seen most clearly at 15°N in Figure 7a) with an amplitude of approximately 1 W/m^2 and wavelength of 30° in longitude. The effect is detectable only near the equator, where solar fluxes are the largest. It is a consequence of the timing of the calculation of the radiative processes in the model.

In ECHAM4, as in many other GCMs, the radiative fluxes are calculated not at every time step (24 min in this case) but every 2 hours. This means that the Sun has 12 discrete noon positions during the day at the centers of 30° longitudinal sectors. In ECHAM4 all layer transmissivities and reflectivities are calculated once every 2 hours for those discrete sun positions and then used to calculate radiative fluxes every time step with different clouds and temperature. Consider such a longitudinal sector and the downward solar flux at the tropopause at the equator, where the Sun is at zenith at the center of the sector. Assume for simplicity that aerosols and the atmosphere are purely absorbing. Then the downward solar flux F is absorbed in the stratosphere by aerosols and gases and at the tropopause:

$$F = S_0 \times \cos\varsigma \times \exp(-\tau_{\text{eff}}) \cong S_0 \times \cos\varsigma \times (1 - \tau_{\text{eff}}) \quad (6)$$

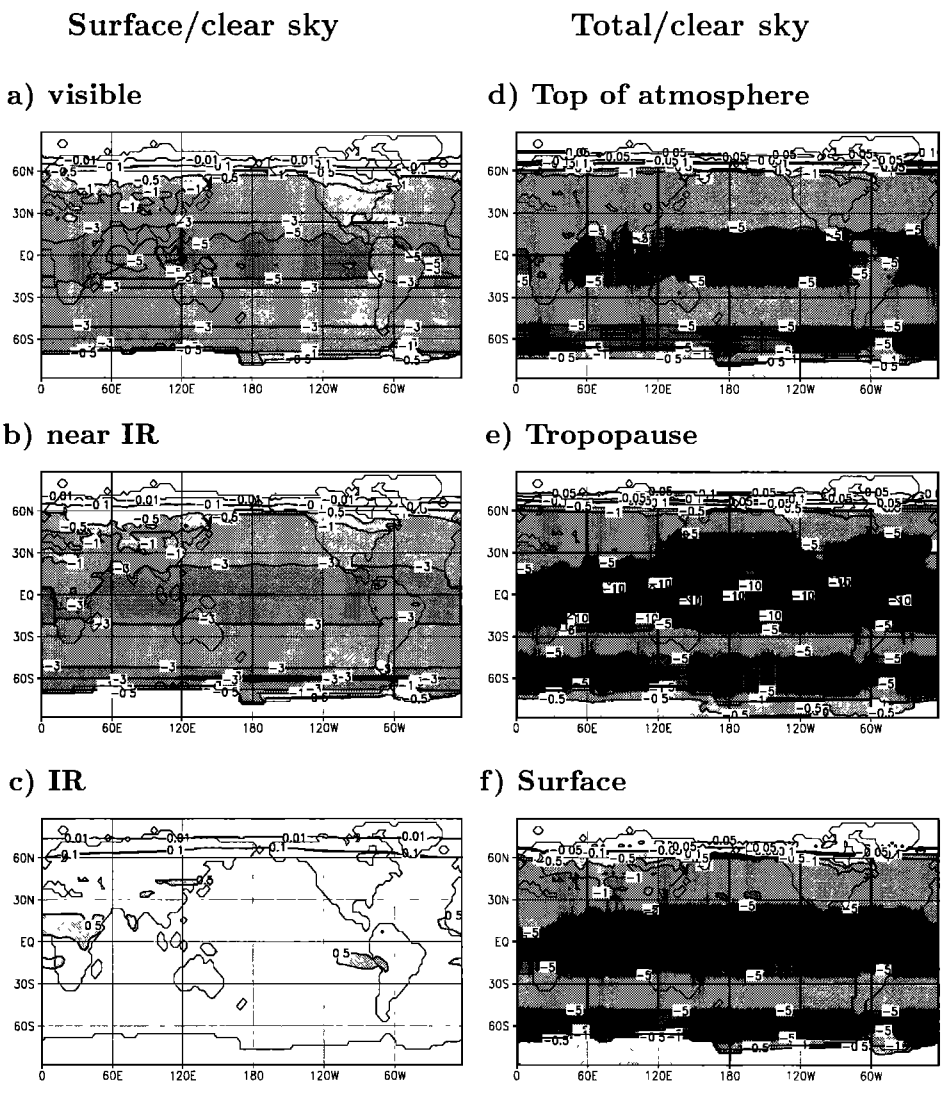

Figure 7. Geographic distribution of monthly averaged changes of (a) visible, (b) near IR, and (c) LW clear-sky fluxes (W/m^2) at surface for January 1992 and changes of total fluxes for (d) top of atmosphere, (e) tropopause, and (f) surface in run C (climatological SST/no aerosol response).

where S_0 is the solar constant. The solar zenith angle ς is corrected every 24 min time step to get an accurate boundary condition for solar radiation at the top of the atmosphere, but the effective optical depth of the aerosol layer

$$\tau_{\text{eff}} = \tau / \cos \varsigma_o \qquad (7)$$

(used in the calculation of the transmissivities and reflectivities in the Morcrette scheme and defined for the sun centered in the longitudinal sector) is fixed for two hours. Here τ is the combined optical depth of the aerosol layer and stratosphere, and ς_0 is the solar zenith angle calculated for the Sun centered in the longitudinal sector. The value ς_0 is different for different locations in the sector and fixed for 2 hours. It is calculated assuming that the Sun is at its zenith at the center of the sector. The value τ_{eff} is smaller for the center of a sector compared with its boundaries, because $\varsigma_0 = 0$ at the center and $\varsigma_0 = 15°$ at the edge of the sector. The difference in τ_{eff} for the center and for the edge of the sector in this case would be equal to

$$\Delta\tau_{\text{eff}} = 0.035 \times \tau . \qquad (8)$$

Although solar zenith angle ς is modified every 24 min, for 2 hours, τ_{eff} is frozen in the layer reflectivity and transmissivity relations, which are used to recalculate the radiative fluxes every time step. This systematic discrepancy in τ_{eff} for a purely absorbing aerosol with an optical depth τ_a=0.1 could produce a systematic error ΔF in solar forcing at the tropopause of

$$\Delta F = S_0 \times \cos\varsigma \times 0.035 \times \tau_a \approx 4.5 \text{ W/m}^2 . \qquad (9)$$

ΔF depends on the aerosol optical depth only, because the optical depth of the clear stratosphere is subtracted when we calculate the forcing.

For scattering aerosols and diurnal averaging, the systematic error is much smaller but still larger than 1 W/m^2 (Figure 7). This systematic error probably exists in clear-sky fluxes in most models which use a large time step for radiation, but it does not influence the dynamics and temperature distribution, because stochastic behavior of clouds reduces this effect for all-sky conditions.

This systematic time approximation error is not related only to aerosols. It works in the same way for gaseous absorption and Rayleigh scattering in the atmosphere. We do not see it in the total flux, because the error is relatively small, but when we look at a small forcing, it becomes obvious.

There is a simple way to avoid this systematic error for clear-sky conditions. One can make it random by using a random longitude of ς_0 within each 30° sector for the calculation of transmissivities and reflectivities at each time step, instead of putting the Sun every time in the center of the sector. However, for all-sky conditions, clouds randomize the radiative fluxes effectively, and we do not see that structure in the all-sky forcing.

5.3 Dependence of Radiative Forcing on State of the Climate System

Figures 8a-8c show the changes of zonal mean all-sky total (visible + near-IR + LW) net radiative flux at the top of the atmosphere, tropopause, and surface produced by the aerosols in run C. The total forcing is a combination of negative solar and positive thermal forcing. In the polar winters, when there is no solar radiation, positive thermal forcing dominates. At the surface the aerosol decreases the incoming radiation to the surface by 4-5 W/m^2 during half a year after the eruption in the tropical region. A significant reduction of incoming radiation of more than 1 W/m^2 lasts until January 1993 and is spread to the midlatitudes. Smaller changes of fluxes are observed at the top of the atmosphere, and larger changes of fluxes are observed near the tropopause.

Figures 8d-8f show the differences in all-sky total (visible + near-IR + LW) zonal mean aerosol radiative forcing at the surface between experiment C (climatological SST, no response to aerosols) and the three other experiments from

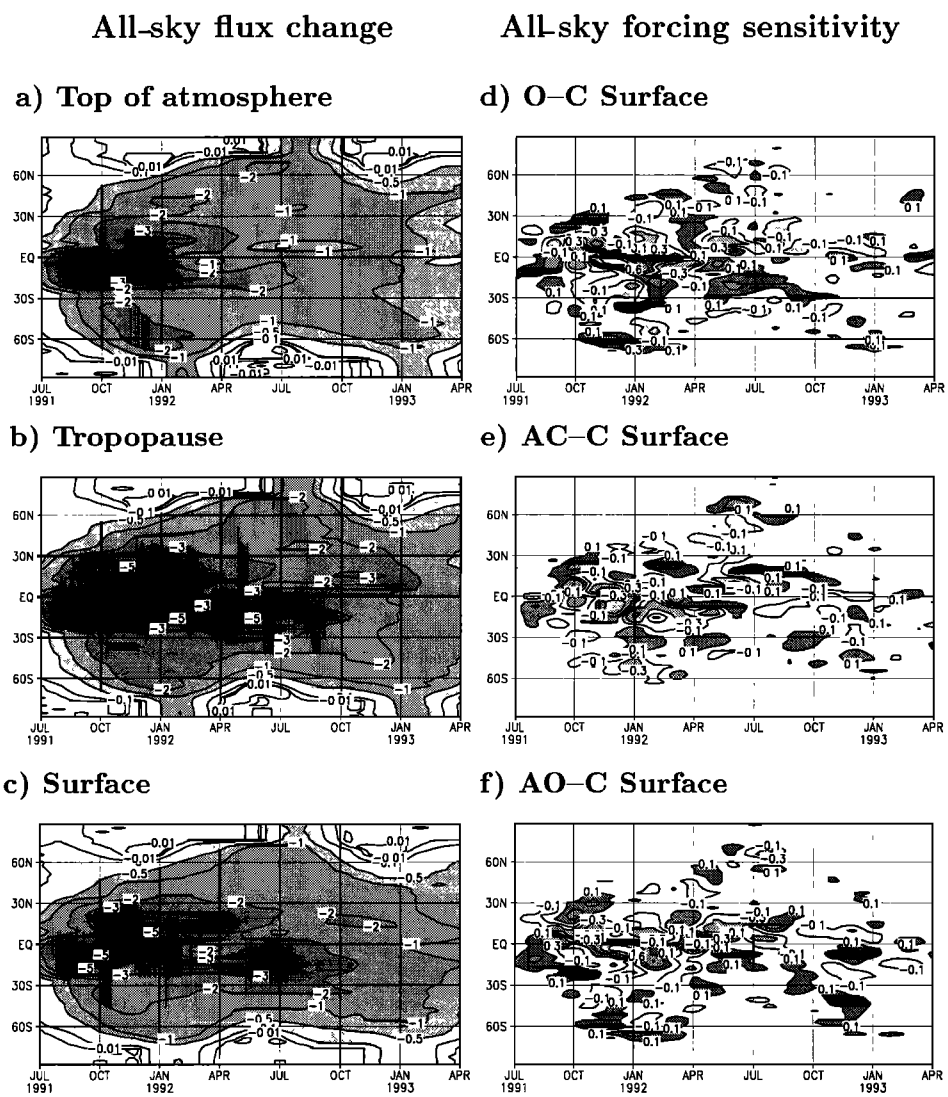

Figure 8. All-sky zonal and monthly averaged total aerosol radiative forcing (W/m^2) for case C (climatological SST/no aerosol response) at (a) the top of atmosphere, (b) tropopause, and (c) surface and the zonal and monthly averaged differences of all-sky total aerosol radiative forcing (W/m^2) at the surface for all the cases from Table 1: (d) O-C, (e) AC-C, and (f) AO-C (c).

Table 1. The differences in forcing between the different experiments shown in Table 1 (compare Figure 8c with Figures 8d-8f), which are caused by different meteorological conditions, are relatively small.

The small random values in Figure 8d means that for the case of Pinatubo aerosols, radiative forcing is insensitive to variations of the meteorological fields in the range of natural climatological variability. It also means that systematic climate reactions to the 1991-1992 El Niño-Southern Oscillation (ENSO) event (particularly enhanced tropical cloudiness) do not bias the calculation of radiative forcing.

The similar pattern in Figure 8e means that even when accounting for the systematic climate response to the Pinatubo aerosol effects (primarily heating of the tropical lower stratosphere and smaller circulation-induced changes) the calculation of radiative forcing is not seriously affected. Since the main effect of the Pinatubo aerosols in the context of forcing is stratospheric heating, it is the LW flux changes that are most strongly affected, and they are an order of magnitude smaller than the solar flux changes. The randomness of the pattern also shows that weather noise is not systematic or large.

Figure 8f also has a pattern of small random differences. In addition to validating the above conclusions, this result shows that there is not a synergistic combination of responses to ENSO and Pinatubo which result in a systematic change of radiative forcing. Because these results are so robust in the comparison of just one realization of each experiment, for this problem we do not see a need for ensemble calculations.

5.4. Dependence of Radiative Forcing on Spectral Interval and on Cloudiness

Figure 9 shows zonal mean forcings calculated for experiment C for different wave bands compared at the surface for clear-sky and all-sky conditions. The clouds significantly affect the aerosol radiative forcing in all the bands, but their impact in the solar bands has a much larger absolute value. The clouds block the solar radiation and reduce the radiative forcing by 1-2 W/m^2 compared with the clear-sky case. The LW forcing is reduced by clouds by almost 50%, because of absorption by water vapor and cloud droplets.

The difference is the largest in the equatorial region with dense cloudiness. This comparison shows that clear-sky forcing is very different energetically than the all-sky forcing and does not characterize the real change of radiative balance of the climate system.

5.5. Comparison With Observations

Global pyranometer measurements at Mauna Loa, Hawaii, at 19°N [*Dutton et al.*, 1992] show that monthly mean clear-sky total solar irradiance decreased by approximately 5% after the Pinatubo eruption and by 2.7% on average for the 10 month period following the eruption. This latter value corresponds to 10-11 W/m^2 clear-sky solar forcing at the surface. We calculated (Figure 9) that the sum of visible and near-IR monthly mean forcings for the same latitude as about 8-9 W/m^2, which is close but slightly less. The elevation of the Mauna Loa Observatory is 3.4 km, however, and this affects the comparison by 1-1.5 W/m^2, practically eliminating the discrepancy.

Minnis et al. [1993] used Earth Radiation Budget Experiment satellite data [*Barkstrom*, 1984] to examine the 40°S-40°N latitude belt from May to October 1991. They showed that for August 1991, at the top of the atmosphere, the reflected shortwave radiation increased by 10 W/m^2, while the downward net radiation decreased by 8 W/m^2 in the 5°S-5°N latitude band. Our calculations give a 10-11 W/m^2 decrease in the net solar flux at the top of the atmosphere in the tropics, because of increasing reflection by the aerosols, a value close to the observations. The outgoing LW flux, however, decreased by 6 W/m^2, which gives a total cooling only 4-5 W/m^2 in comparison with 8 W/m^2 in observations. The forcing is stronger in the observations, because of the including of the stratospheric temperature response in the forcing, which was calculated as the difference of the fluxes after and before the Pinatubo eruption [*Minnis et al.*, 1993]. The observations [*Angell*, 1993; *Labitzke and McCormick*, 1992] and our simulations show that after correction for quasi biennial oscillation (QBO) and ozone depletion effects, the Pinatubo aerosol causes increases in stratospheric temperature of 3°-4°C. This increases the outgoing LW flux by approximately 2 W/m^2, which improves the comparison of the observed and calculated forcings. This result demonstrates how in this case radiative forcing is sensitive to its definition.

5.6. Vertical Distribution of Heating Rates

Figure 10 shows the zonal mean radiative heating in the visible, near-IR, LW, and total heating for August 1991, January 1992, August 1992, and April 1993. The forcing in the visible is limited to a small reduction of heating in the upper stratosphere, because of less ozone absorption of ultraviolet radiation backscattered by the aerosols. In contrast to *Kinne et al.* [1992], solar forcing in the near IR contributes substantially to the total stratospheric heating. In the near IR there is also a small cooling caused by less absorption by the water vapor in the troposphere. In the LW there is heating in the lower stratosphere from enhanced absorption in the aerosol layer of upward terrestrial longwave radiation. The enhanced downward LW from the aerosol cloud also produces enhanced absorption by H_2O and CO_2 in the troposphere. Even in the case that allows response to the aerosols, the reduced upward longwave from a cooler surface would be more than compensated by the much larger stratospheric heating, thus still producing a small tropospheric heating.

In August 1991 and January 1992 the maximum near-IR aerosol heating is at a much higher altitude than the region of maximum LW heating and reaches 0.2-0.3 K/d. The maximum LW heating has the same strength. The maximum total (visible + near-IR + LW) aerosol heating is located at the 30-40 mbar level in the equatorial region and until August 1992 is more than 0.3 K/d, which is in a good agreement with *Kinne et al.* [1992] but 1.5-2 times larger than estimated by *Shibata et al.* [1996]. By April 1993 it decreases to 0.1 K/d. In August 1991 and January 1992 the near-IR heating at 30-40 mbar is half the LW rate, but in August 1992 and April 1993, the maximum of near-IR heating goes to the same level and has the same value as the LW rate because of the decreasing of the aerosol optical depth.

In contrast with other authors [*Kinne et al.*, 1992; *Shibata et al.*, 1996; *Lacis et al.*, 1996] we calculate more significant stratospheric heating in the near IR. In contrast to the above papers we do not use a fixed or column mean effective radius

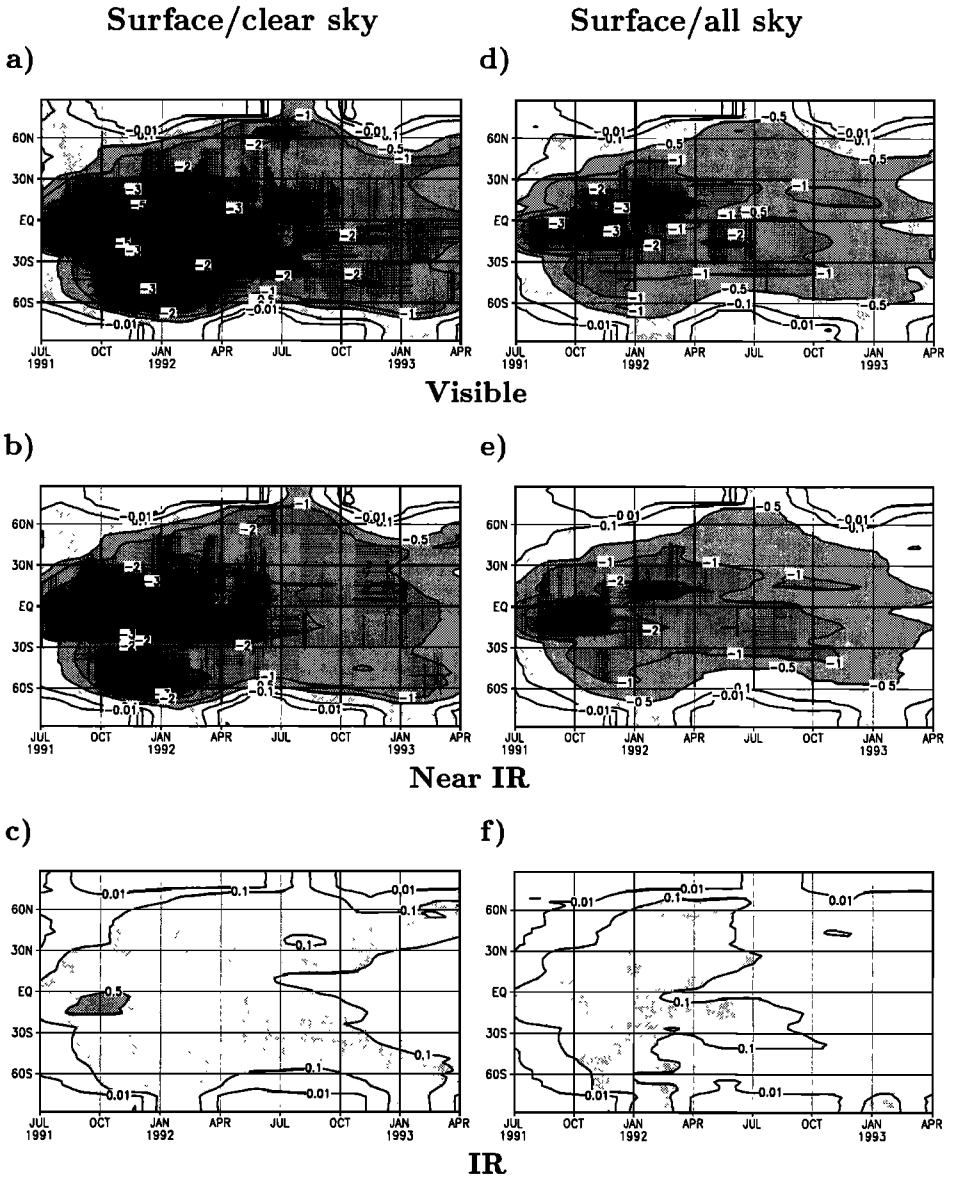

Figure 9. Zonal and monthly averaged changes at the surface of (a) visible, (b) near IR, and (c) LW clear-sky fluxes (W/m^2) caused by the Pinatubo aerosols and the same for the all-sky flux changes in the (d) visible, (e) near IR, and (f) LW, all for run C.

but account for its variations with altitude. As a result, we can resolve small particles at the top of the aerosol layer with $r_{eff} \approx 0.25$ μm (Figure 2). For particles small in comparison with wavelength the single-scattering albedo goes to zero in proportion to the volume of the particle [*van de Hulst*, 1981]. The asymmetry parameter goes to zero as well in the asymptotic regime of small particles. We can see these effects in our results in the middle near IR for $\lambda = 2.5$ μm, for example. More absorbing small particles produce near-IR heating at the top of the aerosol cloud at the beginning of the process. When the maximum effective radius decreases, the near-IR heating goes down in the region closer to the core of the cloud.

6. Estimation of Errors in Forcing Calculations

The problems of the accuracy of radiative calculations in climate models and of climate forcing calculations are fundamental. Unfortunately, they cannot be just resolved by simple numerical tests, which is the typical situation in climate-related studies. They involve a series of inherent uncertainties of our knowledge about the climate system, for example, the distribution and optical properties of clouds, or the accuracy and coverage of available observations.

In our study we improved the characterization of aerosol radiative parameters by combining SAGE-II-observed aerosol extinction and UARS-retrieved effective radii. We calculated radiative forcing with the ECHAM4 GCM using Delta-Eddington-type radiative transport algorithm [*Fouquart and Bonnel*, 1980]. There is a long list of studies of radiative forcing with the Delta-Eddington algorithm, including, just recently, *Kinne et al.* [1992], *Pollack et al.* [1993], and *Shibata et al.* [1996]. We use the calculated forcing (or aerosol parameters) as input into calculations of climate response with our GCM, which provides an a posteriori test for the input aerosol parameters.

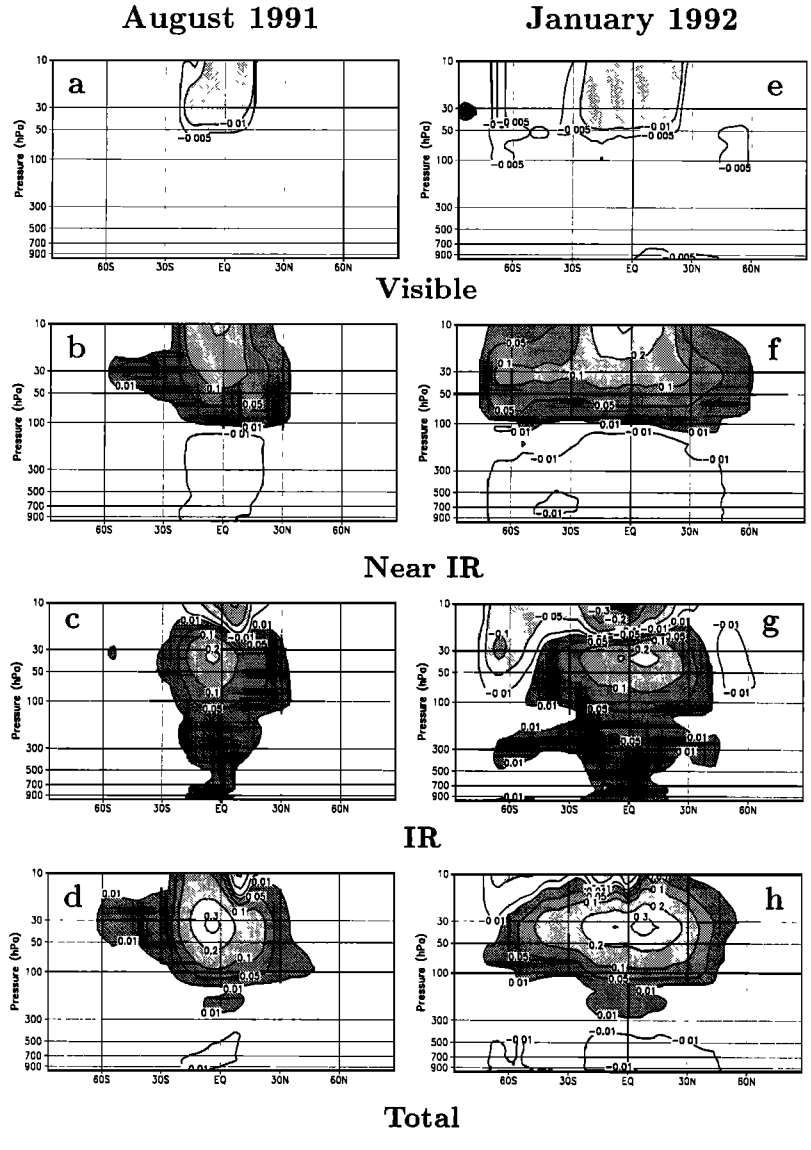

Figure 10. Zonal and monthly averaged perturbations of the atmospheric radiative heating rates (K/d) caused by the Pinatubo aerosols for August 1991 for (a) the visible, (b) near IR, (c) LW, and (d) total; for January 1992 for (e) the visible, (f) near IR, (g) LW, and (h) total; for August, 1992 for (i) the visible, (j) near IR, (k) LW, and (l) total; and for April 1993 for (m) the visible, (n) near IR, (o) LW, and (p) total.

There are three main sources of errors in the calculation of radiative forcing.

Delta-Eddington schemes [*Joseph et al.*, 1976] are not very accurate for optically thin scattering layers. The accuracy of such algorithms has been discussed for more than 20 years [*Meador and Weaver*, 1980; *King and Harshvardhan*, 1986; *Li and Ramaswamy*, 1996]. The Delta-Eddington algorithm is well tested by comparison with referenced highly accurate schemes. As shown by *Li and Ramaswamy* [1996] and *King and Harshvardhan* [1986], the errors of the Delta-Eddington algorithm for a thin scattering layer are up to 20% for reflection, 2-3% for transmission, and up to 10% for absorption.

Uncertainties due to insufficient or inaccurate input information (e.g., aerosol characteristics, cloud distribution, and radiative properties) into radiative transfer calculations cause additional errors in forcing calculations. This type of error cannot be evaluated by applying a highly accurate reference radiative transfer algorithm like the discrete ordinate model (DISORT) [*Stamnes et al.*, 1988]. The estimated accuracy of SAGE II extinction for 1.02 μm is 15-20% [*Thomason et al.*, 1997]. Effective radius is defined with the accuracy of 4-6% [*Grainger et al.*, 1995]. The accuracy of Mie calculations and spectral averaging is not less than 5-10%.

Forcing depends on meteorological conditions and therefore exhibits some random variations. We calculated radiative forcing for four different meteorological fields. Differences in the meteorological parameters were caused by different SSTs and by the atmospheric response to the aerosol radiative effect. The calculated differences in the forcing are of the order of 10% (Figure 8). This means that meteorological noise changes the forcing by only 10% and is capable of changing the forcing only slightly. This result

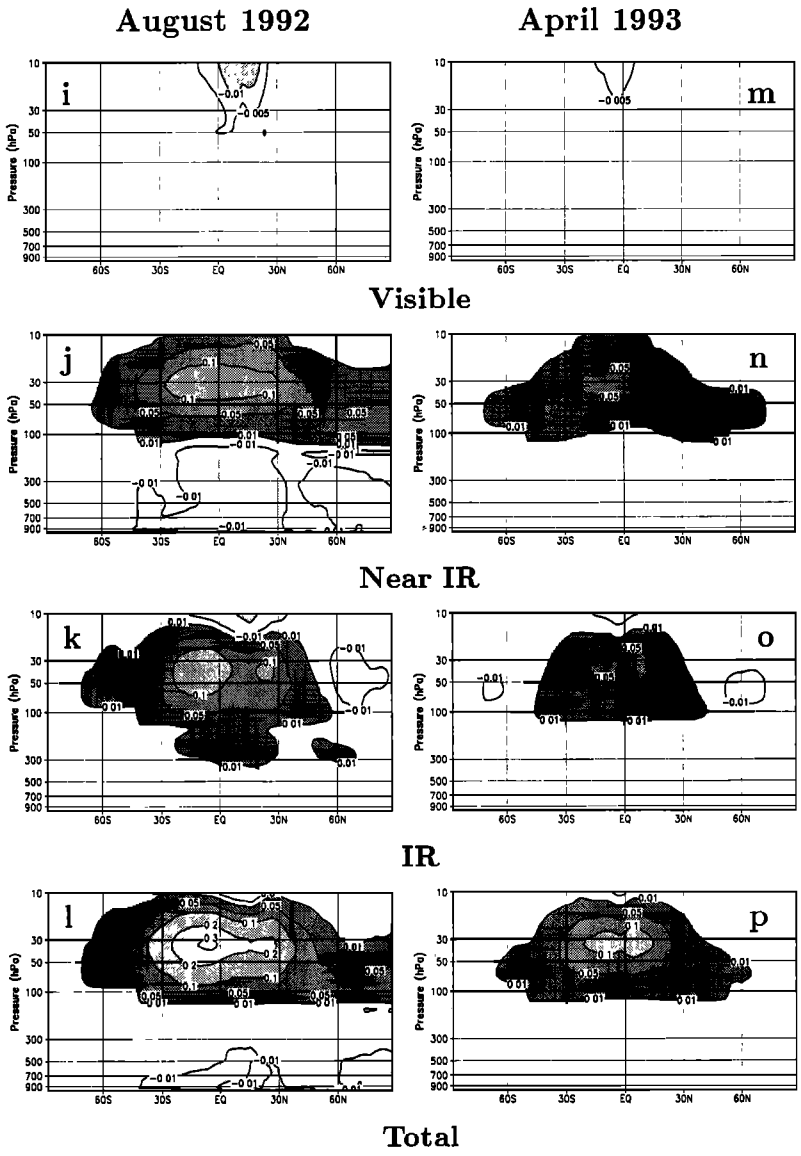

Figure 10. (continued)

confirms that our forcing definition makes sense and gives a natural scale for estimating the numerical accuracy of the forcing calculations.

For estimation of the overall accuracy of the forcing calculations, it is important that numerical errors in radiative transfer calculations are systematic. Therefore a numerical error in the forcing is of the same order or even less than in the fluxes when we calculate the forcing as the difference between fluxes with and without aerosol. We estimate the overall relative error in solar forcing to have a maximum potential value of 20%. Solar radiation does not contribute much to the atmospheric heating but mostly changes the downward radiative fluxes at surface. Longwave radiation produces more than 80% of the stratospheric heating and contributes very little to the change of the surface radiative balance. Numerical errors in longwave forcing for optically thin layers are smaller than for solar radiation and do not exceed 5%. Therefore accounting for the relative role of solar and longwave contributions to the total forcing, we conclude that the possible error related to radiative transfer calculations is about 5% for atmospheric heating and 15% for the surface radiative balance. The overall effect of the two other factors, natural variability and uncertainties in atmospheric radiative parameters, caused by observation and retrieval errors, incomplete coverage, errors in cloud distribution, and radiative properties, is of the order of 20%. Therefore the accuracy of the Delta-Eddington algorithm at this time is not a limiting factor for the calculation of aerosol radiative forcing, but could be in the future. In order to improve the accuracy, better observations and quantification of aerosol parameters are probably more important.

7. Discussion and Conclusions

1. On the basis of the SAGE II extinctions and UARS-retrieved effective radii we have developed a zonal and monthly mean 2-year Pinatubo aerosol spectral data set suitable for use in GCM experiments to study the climatic effects of the largest eruption so far of the 20th century. The forcing calculation with this data set provides a good test for the evaluation of aerosol parameters. The forcing field is an important characteristic of the Pinatubo aerosol cloud.

2. We have calculated aerosol radiative forcing for three main purposes: to evaluate our aerosol data set, to estimate perturbations of the Earth's radiative balance, and to analyze the input to our ECHAM4 climate response calculations. The complete specification of radiative forcing must include the vertical distribution of atmospheric heating rates and the change of downward thermal and net solar radiative fluxes at the surface. These data would be enough to prescribe the forcing for a GCM which does not include aerosol effects in the radiative code.

3. The calculated aerosol radiative forcing is in good agreement with satellite- and ground-based observations. It is stronger than -6 W/m^2 at the surface over large areas and significantly disturbs the Earth's radiative balance.

4. Aerosol radiative forcing is insensitive to climate variations. The forcings calculated in four different experiments are quite close, except in the regions with changed dense clouds. Because clouds decrease monthly mean radiative forcing by 20-40%, instant effect of clouds could be much larger. Cloud optical properties and distributions therefore would be an important reason for discrepancies between different models. This problem needs special consideration and intercomparison studies.

5. Solar forcing in the near IR ($0.68\ \mu m < \lambda < 4\ \mu m$) contributes significantly to stratospheric heating. This is because of absorption of near-IR radiation by small particles at the top of the aerosol cloud. It is important to include this effect as well as to use vertically resolved aerosol characteristics to understand the climatic response to volcanic aerosols.

6. The aerosol radiative forcing calculation is a severe test for a radiative model. The results discussed here are based on the modified Morcrette scheme used in the ECHAM4 environment. It is a well-tested radiative scheme used in the state-of-the-art GCMs at the Max Planck Institute and at ECMWF. It has a low spectral resolution, however, which can affect the results, in spite of the accurate averaging of aerosol parameters to the broadband intervals of the model.

7. In calculations with the ECHAM4 model we found a systematic time approximation error in the solar clear-sky radiation fluxes of the order of 1 W/m^2. The model probably amplifies the effects of multiple scattering of solar radiation between the model layers, especially for the cases with dense cloudiness and high surface albedo. The model includes tropospheric aerosols, which increase the effective reflection from the surface, particularly over the Sahara. These effects slightly decrease the aerosol radiative forcing.

8. To more accurately investigate the model-dependent effects, we conducted preliminary forcing calculations with the radiative model used in the Goddard Earth Observing System (GEOS) GCM [*Chou*, 1992; *Chou and Suarez*, 1994; *Takacs et al.*, 1994] with higher spectral (21 spectral interval) and vertical resolution. With this model we obtained results very close to what we obtain from the Morcrette scheme. We plan to continue this study to make a complete comparison between the forcing calculated with these two different models.

9. We would be happy to provide these forcing and aerosol data for GCM experiments at any spatial and spectral resolution upon request.

Acknowledgments. We thank David Rind for valuable discussions of the paper. This work is supported by NASA grants NAG 5-1835 and NAGW-4912 and NSF grant ATM-9528201. Part of the work was performed during visits of G. Stenchikov and A. Robock to MPI and of I. Kirchner and H.-F. Graf to the University of Maryland. These visits were partially supported by the Max Planck Society and the VW Foundation. The GCM simulations were performed under grant 07 VSK 01 of BMBF. R. G. Grainger and A. Lambert were supported by the UK Natural Environmental Research Council.

References

Angell, J. K., Comparison of stratospheric warming following Agung, El Chichon and Pinatubo volcanic eruptions, *Geophys. Res. Lett.*, *20*, 715-718, 1993.

Angell, J. K., and J. Korshover, Comparison of stratospheric warming following Agung and El Chichon, *Mon. Weather Rev.*, *111*, 2129-2135, 1983.

Ansmann, A., F. Wagner, U. Wandinger, I. Mattis, U. Gorsdorf, H.-D. Dier, and Jens Reichardt, Pinatubo aerosol and stratospheric ozone reduction: Observations over central Europe, *J. Geophys. Res.*, *101*, 18,775-18,785, 1996.

Antuña, J. C., Mount Pinatubo stratospheric aerosol decay during 1992 and 1993, as seen by Camagüey lidar station, in *The Mount Pinatubo Eruption: Effects on the Atmosphere and Climate*, edited by G. Fiocco, D. Fuà, and G. Visconti, pp. 4-9, Springer-Verlag, New York, 1996.

Antuña, J. C. and M. Sorochinski, Measurement of stratospheric aerosols at Camagüey during 1992, (in Spanish), *Geofís. Int.*, *34*, 143-145, 1994.

Avdyushin, S. I., G. F. Tulinov, M. S. Ivanov, B. N. Kuzmenko, I. R. Mezhuev, B. Nardi, A. Hauchecorne, and M. L. Chanin, 1, Spatial and temporal evolution of the optical thickness of the Pinatubo aerosol cloud in the northern hemisphere from a network of ship-borne and stationary lidars, *Geophys. Res. Lett.*, *20*, 1963-1966, 1993.

Baran, A. J., and J. S. Foot, A new application of the operational sounder HIRS in determining a climatology of sulfuric acid aerosol from the Pinatubo eruption, *J. Geophys. Res.*, *99*, 25,673-25,679, 1994.

Barkstrom, B. R., The Earth Radiation Budget Experiment (ERBE), *Bull. Am. Meteorol. Soc.*, *65*, 1170-1185, 1984.

Bluth G. J. S., S. D. Doiron, S. C. Schnetzler, A. J. Krueger, and L. S. Walter, Global tracking of the SO_2 clouds from the June 1991 Mount Pinatubo eruptions. *Geophys. Res. Lett.*, *19*, 151-154, 1992.

Chou, M. D., A solar radiation model for use in climate studies, *J. Atmos. Sci.*, *49*, 762-772, 1992.

Chou, M. D., and M. J. Suarez, An efficient thermal infrared radiation parameterization for use in general circulation models, in Technical Report Series on Global Modeling and Data Assimilation, vol. 3, NASA Tech. Mem. 104606, 85 pp., 1994.

d'Almeida, G. A., P. Koepke, and E. P. Shettle, Atmospheric aerosols, in *Global Climatology and Radiative Characteristics*, 561 pp , A. Deepak, Hampton, Va., 1991.

Davies, C. N., Size distribution of atmospheric particles, *J. Aerosol Sci.*, *5*, 293-300, 1974.

DeFoor, T. E., E. Robinson, and S. Ryan, Early observations of the June 1991 Pinatubo volcanic plume over Mauna Loa Observatory, Hawaii, July, 1991-November, 1991, *Geophys. Res. Lett.*, *19*, 187-190, 1992.

Deshler, T., D. J. Hofmann, B. J. Johnson and W. R. Rozier, Balloonborne measurements of the Pinatubo aerosol size distribution and volatility at Laramie, Wyoming during the summer of 1991, *Geophys. Res. Lett.*, *19*, 199-202, 1992.

Deshler, T., B. J. Johnson, and W. R. Rozier, Balloonborne measurements of Pinatubo aerosol during 1991 and 1992 at 41°N: Vertical profiles, size distribution, and volatility, *Geophys. Res. Lett.*, *20*, 1435-1438, 1993.

Deutsches Klimarechenzentrum, Modelbetreuungsgruppe, *The ECHAM3 Atmospheric General Circulation Model*, report 6, revision 2, 190 pp., Max-Planck-Inst. für Meteorol., Hamburg, Germany, 1993.

Di Girolamo, P., G. Pappalardo, N. Spinelli, V. Beratdi, R. Velotta, Lidar observations of the stratospheric aerosol layer over southern Italy in the period 1991-1995, *J. Geophys. Res.*, *101*, 18,765-18,773, 1996.

Dutton, E. G., and J. R. Christy, Solar radiative forcing at selected locations and evidence for global lower tropospheric cooling

following the eruption of El Chichon and Pinatubo, *Geophys. Res. Lett.*, *19*, 2313-2316, 1992.

Dutton, E. G., P. Reddy, S. Ryan, and J. J. DeLuisi, Features and effects of aerosol optical depth observed at Mauna Loa, Hawaii: 1982-1992, *J. Geophys. Res.*, *99*, 8295-8306, 1994.

Eluszkiewicz, J., et al., Residual circulation in the stratosphere and lower mesosphere as diagnosed from microwave limb sounder data, *J. Atmos. Sci.*, *53*, 217-240, 1996.

Fouquart, Y., and B. Bonnel, Computations of solar heating of the Earth's atmosphere: A new parameterization, *Beitr. Phys. Atmos.*, *53*, 35-62, 1980.

Frolkis, V. A., and E. V. Rozanov, Radiation code for climate and general circulation models, in *Proceedings of the International Symposium on Radiation*, pp. 176-179, A. Deepak, Hampton, Va., 1993.

Gates, W. L., AMIP: The Atmospheric Model Intercomparison Project, *Bull. Am. Meteorol. Soc.*, *73*, 1962-1970, 1992.

Giorgetta, M., and M. Wild, *The Water Vapour Continuum and Its Representation in ECHAM4*, report 162, 38 pp., Max-Planck-Inst. für Meteorol., Hamburg, Germany, 1995.

Goodman, J., K. G. Snetsinger, R. F. Pueshel, and S. Verma, Decay of Mount Pinatubo volcanic perturbation, *Geophys. Res. Lett.*, *21*, 1129-1132, 1994.

Graf, H.-F., I. Kirchner, A. Robock, and I. Schult, Pinatubo eruption winter climate effects: Model versus observations, *Clim. Dyn.*, *9*, 81-93, 1993.

Grainger, R. G., A. Lambert, F. W. Taylor, J. J. Remedios, C. D. Rodgers, M. Corney, and B. J. Kerridge, Infrared absorption by volcanic stratospheric aerosols observed by ISAMS, *Geophys. Res. Lett.*, *20*, 1283-1286, 1993.

Grainger R. G., A. Lambert, C. D. Rogers, F. W. Taylor, and T. Deshler, Stratospheric aerosol effective radius, surface area and volume estimated from infrared measurements, *J. Geophys. Res.*, *100*, 16,507-16,518, 1995.

Grant, W. B., et al., Observations of reduced ozone concentrations in the tropical atmosphere after the eruption of Mt. Pinatubo, *Geophys. Res. Lett.*, *19*, 1109-1112, 1992.

Hansen, J., I. Fung, A. Lacis, D. Rind, S. Lebedeff, R. Ruedy, G. Russell, and P. Stone, Global climate changes as forecast by the Goddard Institute for Space Studies three-dimensional model, *J. Geophys. Res.*, *93*, 9341-9364, 1988.

Hansen, J., A. Lacis, R. Ruedy, and M. Sato, Potential climate impact of the Mount Pinatubo eruption, *Geophys. Res. Lett.*, *19*, 215-218, 1992.

Haywood, J. M., V. Ramaswamy, and L. J. Donner, A limited-area-model case study of the effects of sub-grid scale variations in relative humidity and cloud upon the direct radiative forcing of sulfate aerosol, *Geophys. Res. Lett.*, *24*, 143-146, 1997.

Hofmann, D. J., and J. M. Rosen, Stratospheric sulphuric acid fraction and mass estimate for the 1982 eruption of El Chichón. *Geophys. Res. Lett.*, *10*, 313-316, 1983.

Houghton, J. T., L. G. Meira Filho, B. A. Callander, N. Harris, A. Kattenberg, and K. Maskell (Eds.) *Climate Change 1995–The Science of Climate Change*, 584 pp., Cambridge Univ. Press, New York, 1996.

Jäger, H., O. Uchino, T. Nagai, T. Fujimoto, V. Freudenthaler, and F. Hamburg, Ground based remote sensing of the decay of the Pinatubo eruption cloud at three northern hemisphere sites, *Geophys. Res. Lett.*, *22*, 607-610, 1995a.

Jäger, H., T. Deshler, and D. J. Hofmann, Midlatitude lidar backscatter conversions based on ballonborne aerosol measurements, *Geophys. Res. Lett.*, *22*, 1729-1732, 1995b.

Joseph, J. H., W. J. Wiscombe, and J. A. Weinman, The Delta-Eddington approximation for radiative flux transfer, *J. Atmos. Sci.*, *33*, 2452-2459, 1976.

King, M. D., and Harshvardhan, Comparative accuracy of selected multiple scattering approximations, *J. Atmos. Sci*, *43*, 784-801, 1986.

Kinne, S., O. B. Toon, and M. J. Prather, Buffering of stratospheric circulation by changing amounts of tropical ozone, A Pinatubo case study, *Geophys. Res. Lett.*, *19*, 1927-1930, 1992.

Kirchner, I., and H.-F. Graf, Volcanos and El Niño: Signal separation in Northern Hemisphere winter, *Clim. Dyn.*, *11*, 341-358, 1995.

Knollenberg, R. G., and D. Huffman, Measurements of the aerosol size distributions in the El Chichón cloud, *Geophys. Res. Lett.*, *10*, 1025-1028, 1983.

Kodera, K., Influence of volcanic eruptions on the troposphere through stratospheric dynamical processes in the Northern Hemisphere, *J. Geophys. Res.*, *99*, 1273-1282, 1994.

Kodera, K., and K. Yamazaki, A possible influence of recent polar stratospheric coolings on the troposphere in the Northern Hemisphere winter, *Geophys. Res. Lett.*, *21*, 809-812, 1994.

Labitzke, K. and M. P. McCormick, Stratospheric temperature increases due to Pinatubo aerosol, *Geophys. Res. Lett.*, *19*, 207-210, 1992.

Labitzke, K., B. Naujokat, and M. P. McCormick, Temperature effects on the stratosphere of the April 4, 1982 eruption of El Chichón, Mexico, *Geophys. Res. Lett.*, *10*, 24-26, 1983.

Lacis, A. A., J. E. Hansen, and M. Sato, Climate forcing by stratospheric aerosols, *Geophys. Res. Lett.*, *19*, 1607-1610, 1992.

Lacis, A. A., B. E. Carlson, and M. I. Mishchenko, A general circulation model (GCM) parameterization of Pinatubo aerosols, in *Proceedings of the Fifth Atmospheric Measurement (ARM) Science Team Meeting*, pp. 151-154, Nat. Tech. Inf. Serv., Springfield, Va., 1996.

Lambert, A., R. G. Grainger, J. J. Remidios, C. D. Rogers, M. Corney, and F. W. Taylor, Measurements of the evolution of the Mt. Pinatubo aerosol cloud by ISAMS, *Geophys. Res. Lett.*, *20*, 1287-1290, 1993.

Lambert A., R. G. Grainger, J. J. Remedios, W. J. Reburn, C. D. Rodgers, F. W. Taylor, A. E. Roche, J. B. Kumer, S. T. Massie, and T. Deshler, Validation of aerosol measurements from the improved stratospheric and mesospheric sounder, *J. Geophys. Res.*, *101*, 9811-9830, 1996.

Lambert, A., R. G. Grainger, C. D. Rogers, F. W. Taylor, L. L. Mergenthaler, J. B. Kumer, and S. T. Massie, Global evolution of the Mount Pinatubo volcanic aerosols observed by the infrared limb-sounding instruments CLAES and ISAMS on the Upper Atmosphere Research Satellite, *J. Geophys. Res.*, *102*, 1495-1512, 1997.

Li, J., and V. Ramaswamy, Four-stream spherical harmonic expansion approximation for solar radiative transfer, *J. Atmos. Sci.*, *53*, 1174-1186, 1996.

Long, C. S., and L. L. Stowe, Using the NOAA/AVHRR to study stratospheric aerosol optical thickness following the Mt. Pinatubo eruption, *Geophys. Res. Lett.*, *21*, 2215-2218, 1994.

Mao, J. and A. Robock, Surface air temperature simulations by AMIP general circulation models: Volcanic and ENSO signals and systematic errors, *J. Clim.*, in press, 1998.

Massie S. T., et al., Validation studies using multiwavelength cryogenic limb array etalon spectrometer (CLAES) observations of stratospheric aerosol, *J. Geophys. Res.*, *101*, 9757-9777, 1996a.

Massie, S. T., T. Deshler, G. E. Thomas, J. L. Mergenthaler, and J. M. Russell III, Evolution of the infrared properties of the Mount Pinatubo aerosol cloud over Laramie, Wyoming, *J. Geophys. Res.*, *101*, 23,007-23,019, 1996b.

Mauldin, L. E., III, N. H. Zaun, M. P. McCormick, J. H. Guy, and W. R. Vaughn, Stratospheric Aerosol and Gas Experiment II instrument: A function description, *Opt. Eng.*, *24*, 307-312, 1985.

McCormick, M. P., SAGE II: An overview, *Adv. Space Res.*, *7*, 219-226, 1987.

McCormick, M. P., and R. E. Veiga, SAGE II Measurements of early Pinatubo aerosols, *Geophys. Res. Lett.*, *19*, 155-158, 1992.

McCormick, M. P., P. Hamill, T, J. Pepin, W. P. Chu, T. J. Swissler, and L. R. Master, Satellite studies of the stratospheric aerosol, *Bull. Am. Meteorol. Soc.*, *60*, 1038-1046, 1979.

McCormick, M. P., W. P. Chu, G. W. Grams, P. Hamill, B. W. Herman, L. R. McMaster, T. J. Pepin, P. B. Russell, H. M. Steel, and T. J. Swissler, High-latitude stratospheric aerosols measured by the SAM II satellite system in 1978 and 1979, *Science*, *214*, 328-331, 1981.

McCormick, M. P., L. W. Thomason, and C. R. Trepte, Atmospheric effects of Mt. Pinatubo eruption, *Nature*, *373*, 399-404, 1995.

Meador , W. E., and W. R. Weaver, Two-stream approximations to radiative transfer in planetary atmospheres: A unified description of existing methods and a new improvement, *J. Atmos. Sci.*, *37*, 630-643, 1980.

Minnis, P., E. F. Harrison, L. L. Stowe, G. G. Gison, F. M. Denn, D. R. Doelling, and W. L. Smith Jr., Radiative climate forcing by the Mount Pinatubo eruption, *Science*, *259*, 1411-1415, 1993.

Morcrette, J.-J., Sur la parameterisation du rayonnement dans les

modeles de la circulation generale atmospherique, Ph.D. dissertation, 630, Univ. of Lille, Lille, France, 1984.

Morcrette, J.-J., and Y. Fouquart, On systematic errors in parameterized calculations of longwave radiation transfer, *Q J. R. Meteorol .Soc., 111*, 691-708, 1985.

Morcrette, J.-J., L. Smith, and Y. Fouquart, Pressure and temperature dependence of the absorption in longwave radiation parameterizations, *Beitr. Phys. Atmos., 59*, 455-469, 1986.

Nardi, B., M. L. Chanin, A. Hauchecorne, S. I. Avdyushin, G. F. Tulinov, M. S. Ivanov, B. N. Kuzmenko, and I. R. Mezhuev, Morphology and dynamics of the Pinatubo layer in the northern hemisphere as detected from a ship-borne lidar, 2, *Geophys. Res. Lett., 20*, 1967-1970, 1993.

Oberbeck, V. R., E F. Danielsen, K. G. Snetsinger, G. V. Ferry, W. Fong, and D. M. Hayes, Effect of the eruption of the El Chichón on stratospheric aerosol size and composition, *Geophys. Res. Lett., 10*, 1021-1024, 1983.

Palmer, K. F., and D Williams, Optical constants of sulfuric acid, Application to the clouds of Venus, *App. Opt., 14*, 208-219, 1975.

Perlwitz, J., and H.-F. Graf, The statistical connection between tropospheric and stratospheric circulation of the northern hemisphere in winter, *J. Clim., 8*, 2281-2295, 1995.

Pollack, J. B., D. Rind, A. Lacis, J. E. Hansen, M. Sato, and R. Ruedy, GCM simulation of volcanic aerosol forcing, I, Climate changes induced by steady-state perturbations, *J. Clim., 6*, 1719-1742, 1993.

Pueschel, R. F., D. F. Blake, K. G. Snetsinger, A. D. A. Hansen, S. Verma, and K. Kato, Black carbon (soot) aerosol in the lower stratosphere and upper troposphere, *Geophys. Res. Lett., 19*, 1659-1662, 1992.

Pueschel, R. F., J. M. Livingston, P. B. Russell, and S. Verma, Physical and optical properties of the Pinatubo volcanic aerosol: Aircraft observations with impactors and suntracking photometer, *J. Geophys. Res., 99*, 12,915-12,922, 1994.

Remsberg, E. E., D. Lavery and B. Crawford Jr., Optical constants for sulfuric and nitric acids, *J. Chem. Eng. Data, 19*, 263-265, 1974.

Robock, A., and J. Mao, Winter warming from large volcanic eruptions, *Geophys. Res. Lett., 19*, 2405-2408, 1992.

Robock, A., and J. Mao, The volcanic signal in surface temperature observations, *J. Clim., 8*, 1086-1103, 1995.

Roche, A. E., J. B Kumer, J. L. Mergenthaler, G A. Ely, W. G. Upliner, J. F. Potter, T. C. James, and L. W. Sterrit, The cryogenic limb array etalon spectrometer (CLAES) on UARS: Experiment description and performance, *J. Geophys. Res., 98*, 10,763-10,775, 1993.

Roeckner, E., Parameterization of cloud radiative properties in the ECHAM4 model. in *Proceedings of the WCRP Workshop on Cloud Microphysics Parameterizations in Global Atmospheric Circulation Models*, WCRP-Rep 90, WMO/TD-713, pp. 105-116, World Clim. Res. Programme, Geneva, 1995.

Roeckner, E., and K. Arpe, AMIP experiments with the new Max Planck Institute for Meteorology model ECHAM4, in *Proceedings of the First International AMIP Scientific Conference*, edited by W. L. Gates, WCRP-92, WMO/TD-732, pp. 307-312, World Clim. Res. Programme, Geneva, 1995.

Roeckner, E., K. Arpe, L. Bengtsson, M. Christoph, M. Claussen, L. Duemenil, M. Ecsh, M. Giogetta, U. Schlese, and U. Schulzweida, in *The Atmospheric General Circulation Model ECHAM4: Model Description and Simulation of Present-Day Climate*, report 218, 90 pp., Max-Planck-Inst. für Meteorol., Hamburg, Germany, 1996.

Rosen, J. M., N. T. Kjome, R. L. McKenzie, and J. B. Liley, Decay of Mount Pinatubo aerosol at midlatitudes in the northern and southern hemispheres, *J. Geophys. Res., 99*, 25,733-25,739, 1994.

Russell, P. B., et al., Pinatubo and pre-Pinatubo optical-depth spectra: Mauna Loa measurements, comparisons, inferred particle size distributions, radiative effects, and relationship to lidar data, *J. Geophys. Res., 98*, 22,969-22,985, 1993.

Russell, P. B., et al., Global to microscale evolution of the Pinatubo volcanic aerosol, derived from diverse measurements and analyses, *J. Geophys. Res., 101*, 18,745-18,763, 1996.

Sato, M., J. E. Hansen, M. P. McCormick, and J. B. Pollack, Stratospheric aerosol optical depths, 1850-1990, *J. Geophys. Res., 98*, 22,987-22,994, 1993.

Schmitt, C., and D. Randall, Effects of surface temperature and clouds on the CO_2 forcing, *J. Geophys. Res., 96*, 9159-9168, 1991.

Shibata, K., O. Uchino, T. Kamiyama, and M. P. McCormick, An estimation of the radiative effect in the stratosphere due to the Pinatubo aerosol, *J. Meteorol. Soc. Jpn., 74*, 763-780, 1996.

Stamnes, K., S. C. Tsay, W. Wiscombe, and K. Jayaweera, A numerically stable algorithm for discrete-ordinate-method radiative transfer in multiple scattering and emitting layered media, *Appl. Opt., 27*, 2502-2509, 1988.

Stein, B., M. Del Guasta, J. Kolenda, M. Morandi, P. Rairoux, L. Stefanutti, J. P. Wolf, and L. Woste, Stratospheric aerosol size distributions from multispectral lidar measurements at Sodankyla during EASOE, *Geophys. Res. Lett., 21*, 1311-1314, 1994.

Stenchikov, G. L., and A. Robock, Effects of Pinatubo aerosol microphysical transformations on aerosol optical parameters and forcing, *Eos Trans. AGU*, 75(44), Fall Meet. Suppl., 101, 1994.

Stendel, M., and L Bengtsson, Toward monitoring the tropospheric temperature by means of a general circulation model, *J. Geophys. Res., 102*, 29,779-29,788, 1997.

Stone, R. S., J. R. Key, E. G. Dutton, Properties and decay of stratospheric aerosols in the Arctic following the 1991 eruptions of Mount Pinatubo, *Geophys. Res. Lett., 20*, 2359-2362, 1993.

Stowe, L. L., Cloud and aerosol products at NOAA/NESDIS, *Paleogeogr. Paleoclimatol. Paleoecol., 90*, 25-32, 1991.

Stowe, L. L., R. M. Carey, and P. P. Pellegrino, Monitoring the Mt. Pinatubo aerosol layer with NOAA/11 AVHRR data, *Geophys. Res. Lett., 19*, 159-162, 1992.

Strong, A. E., and L. L. Stowe, Comparing stratospheric aerosols from El Chichon and Mount Pinatubo using AVHRR data, *Geophys. Res. Lett., 20*, 1183-1186, 1993.

Takacs, L. L., A Molod, and T Wang, Documentation of the Goddard Earth Observing System (GEOS) general circulation model - Version 1, NASA Tech. Memo. 104606, vol. 1, 100 pp., 1994.

Tegen, I., A. A. Lacis, and I. Fung, The influence on climate forcing of mineral aerosol from disturbed soils, *Nature, 380*, 419-422, 1996.

Thomason, L. W., A diagnostic aerosol size distribution inferred from SAGE II measurements, *J. Geophys. Res., 96*, 22,501-22,508, 1991.

Thomason, L. W., G. S. Kent, C. R. Trepte, and L. Poole, A comparison of the stratospheric aerosol background periods of 1979 and 1989-1991, *J. Geophys. Res., 102*, 3611-3616, 1997.

Torres, O., J. R Herman, P. K. Bhartia, and Z Ahmand, Properties of Mount Pinatubo aerosols as derived from Nimbus 7 total ozone mapping spectrometer measurements, *J. Geophys. Res., 100*, 14,043-14,055, 1995

Trepte, C. R., R. E. Veiga, and M. P. McCormick, The poleward dispersal of the Mount Pinatubo volcanic aerosol, *J. Geophys. Res., 98*, 18,563-18,573, 1993.

Valero, F. P. J., and P. Pilewskie, Latitudinal survey of spectral optical depths of Pinatubo volcanic cloud - Derived particle sizes, columnar mass loadings, and effects on planetary albedo, *Geophys. Res. Lett., 19*, 163-166, 1992.

van de Hulst, H. C., *Light Scattering by Small Particles*, 470 pp., Dover, Mineda, N. Y., 1981.

Veiga, R. E., SAGE II measurements of volcanic aerosols, in *1993 Tech. Dig. Ser.*, vol. 5, pp. 467-470, Opt. Soc. of Am., Washington, D. C., 1993.

Winker, D. M., and M. T. Osborne, Airborne lidar observations of the Pinatubo volcanic plume, *Geophys. Res. Lett , 19*, 167-170, 1992.

Wiscombe, W., Improved Mie scattering algorithms, *Appl. Opt., 19*, 1505-1509, 1980.

World Climate Research Programme, *Report of the expert meeting on aerosols and their climatic effects*, edited by A. Deepak and H. E. Gerber, WCP-55, 101 pp., Geneva, 1983.

Yue, G. K., L. R. Poole, P.-H. Wang, and E. W. Chiou, Stratospheric aerosol acidity, density, and refractive index deduced from SAGE II and NMC temperature data, *J. Geophys. Res., 99*, 3727-3738, 1994.

J. C. Antuña, A. Robock, and G. Stenchikov (corresponding author), Department of Meteorology, University of Maryland, College Park, MD 20742. (e-mail: antuna@atmos.umd.edu, robock@envsci.rutgers.edu, gera@atmos.umd.edu)

H.-F. Graf and I. Kirchner, Max Planck Institute for Meteorology, Hamburg, Germany. (e-mail: graf@dkrz.de, kirchner@dkrz.de)

R. G. Grainger and Alyn Lambert, Atmospheric, Oceanic and Planetary Physics, University of Oxford, Oxford, England. (e-mail: d.grainger@phys.canterbury.ac.nz, alambert@eos.ucar.adu)

L. Thomason, NASA Langley Research Center, Hampton, VA 23665. (e-mail: l.w.thomason@larc.nasa.gov)

(Received March 20, 1997; revised February 19, 1998; accepted February 23, 1998)